Use of Noise power Spectra (NPS) for Quality Control in Digital Radiography

by

Mohadese Ghorbanzade

A Thesis submitted to the Faculty of Graduate Studies of

The University of Manitoba

in partial fulfillment of the requirements of the degree of

MASTER OF SCIENCE

Department of Physics and Astronomy

University of Manitoba

Winnipeg, Manitoba, Canada

Abstract

Quality control (QC) guidance documents recommend various tests for evaluation of different parameters of x ray imaging systems' performance. QC tests can be time consuming, user-dependent and require specialized tools. The aim of this thesis is to investigate the noise power spectrum (NPS) as a QC constancy test which is simple, fast and lends itself easily to automated analysis. Uniform images were acquired under different conditions representing deviations from ideal performance using two digital x-ray systems. The stationarity and ergodicity of the noise was assessed. The normalized NPS (NNPS) were calculated using the methodology of the international electrotechnical commission. The total relative difference was used to quantify the changes in the NNPS.

The NNPS was computed for images: with focal spot blooming, collected using large and small focal spot (to mimic resolution change), various tube voltage values, with and without defective pixels, with residual image and with a mismatched anti-scatter grid. Results showed that the NPS method is not sensitive to image lag and focal spot blooming investigated in this study. However, the NPS method was sensitive to changes in resolution introduced by changing the focal spot size, kV deviations as small as 1 kV, defective pixels representing 0.01% of the image pixel and 0.98 MSE difference from the original image, affixed pattern artifacts and a mismatched grid.

The NPS was decomposed into its components (fixed pattern, quantum and electronic) to investigate the effect of different performance deviations on the NPS components. The negligibility of the electronic noise was verified. The results showed the fixed pattern changes impacted the fixed pattern NPS component the most and the changes associated with quantum noise affected the quantum component.

This thesis suggests the NPS is sensitive to a variety of deviations in system parameters and performance metrics likely to arise in the quality control of digital radiography systems. NPS decomposition can further help identify the source of deviations. The NPS has the potential to be used as a constancy test for routine quality control of DR systems.

Acknowledgements

I would like to express my sincere and warm gratitude to my supervisor, Dr. *Idris Elbakri*, for his continuous support of my M.Sc. study and research, and for his patience and encouragement. In addition, I would like to thank *CancerCare Manitoba Foundation* for the funding provided during this work.

To my committee, *Dr. Stephen Pistorius* and *Dr. Meredith Brownlee*, I am profoundly grateful for your suggestions and feedback throughout my project.

Special Thanks to my brothers, *Mahdi and Alireza*, and my friends for their unconditional support and love during this time.

I am very much indebted to my partner, *Dr. Ramin Naseri Oskouie*, for being my constant source of inspiration and encouragement throughout my study. Thank you from the bottom of my heart for your love, faith and patience.

Finally, I would like to dedicate this thesis to my *mom* and *dad*. I miss you every day.

Contents

List of Figures

List of Tables

List of Abbreviations

DR	Digital Radiography
ALARA	As Low As Reasonably Achievable
QC	Quality Control
NPS	Noise Power Spectrum
CR	Computed Tomography
TFT	Thin Film Transistors
CCD	Charged Couple Device
AEC	Automatic Exposure Control
HVL	Half Value Layer
SNR	Signal-to-Noise Ratio
MTF	Modulation Transfer Function
CNR	Contrast-to-Noise Ratio
SDNR	Signal Difference-to-Noise Ratio
ROI	Region Of Interest
TRD	Total Relative Difference
IEC	International Electrotechnical Commission
WSS	Wide Sense Stationary
NNPS	Normalized Noise Power Spectrum
MSE	Mean Squared Error
COV	Coefficient Of Variation

Chapter 1

Introduction and Background

1.1 Introduction

X ray imaging is the most commonly used imaging modality in medicine and has the largest contribution of man-made radiation exposure to population [1]. More than 20 million diagnostic x ray procedures are performed each year in Canada [2]. Over the past two decades, digital imaging has dominated the x ray imaging field and most of the radiology departments in main hospitals have become completely digitized [3],[4]. Digital technology produces an immediate preview of the image and decreases acquisition time. It also reduces radiation dose without compromising image quality due to the wider dynamic range of the detector. Other advantages of digital radiography (DR) systems include decreased repeat rate, quick image sharing, ability to archive images electronically, higher patient throughput and image post-processing [5]. Despite these advantages, DR systems expose patients to risks of ionizing radiation. Therefore, DR systems must be operated in accordance with the fundamental radiation protection principle known as the ALARA (as low as reasonably achievable) [6]. Any suboptimum imaging procedure can also result in the suppression of the clinical value of the image and obscure an accurate diagnosis [7]. Thus, there must be a consistent investigation of imaging system performance to avoid unnecessary exposure to individuals and maintain an optimal image quality. This can be achieved by implementing a quality control (QC) program [1]. QC is defined as a reactive process that is performed in order to identify any defect or degradation in the system [8]. Health Canada defines x ray imaging systems QC program as “a series of standardized tests which are developed in order to diagnose changes in all parts of imaging chain. These tests must be carried out routinely to avoid any degradation in the quality of the x ray image and over-exposure to patients”.

Chapter 1. Introduction and Background

Key personnel in the imaging department that are involved in the QC procedure include the x ray technologist, radiologist and medical physicist [8]. The QC procedure is performed by the x ray technologist. The medical physicist is involved with the design and implementation of the QC program, troubleshooting and evaluation of the system equipment on a regular basis [8].

A QC program in radiology usually involves testing of different components of the system with appropriate frequency [5]. These components include various parts of the imaging chain including x ray generation, detection and image display. Any clinically significant deviation in each of these parts' performance must be detected in the QC procedure. For this purpose, assessment of image quality parameters like spatial resolution, contrast, noise and systematic artefacts must be included in the QC program. Another important aspect of a QC program is the stability of radiation output and x ray generation. Various methods are recommended for evaluation of each of the DR system performance parameters. These methods involve complex tasks and specialized tools. Carrying out these tests can be time consuming and error prone. Moreover, current methods are user dependent and may not be performed in a reproducible fashion every time. In this study, our goal is to evaluate the noise power spectrum (NPS) as constancy test which is simple, fast and lends itself easily to automated analysis.

NPS is used to characterize the noise content of the image. It describes the frequency-dependent response of the imaging system to the noise input [9]. Determining the NPS requires the use of well-known computational methods applied to uniform images. NPS calculation is simple, fast and does not require manufacturing and alignment of a test object. Noise in digital x ray imaging consists of three components: quantum, electronic and fixed pattern. Each of these components corresponds to one or more stages of the imaging chain. Therefore, measuring the NPS can be a useful test of system performance. All being said, the NPS is not typically used as a QC tool for DR systems. This is due to the fact that QC tests are commonly carried over from the era of conventional radiography and the fact that the NPS requires complex calculations.

In this study, we evaluate the NPS as a constancy test which is sensitive to changes or degradations in system performance such as exposure fluctuations, focal spot size blooming, resolution loss and detector defects. Since the NPS can be decomposed into its components, we will investigate if NPS decomposition can help identify which component of the noise is mostly affected and therefore focus troubleshooting efforts in case of a suspected performance deviation.

Chapter 1. Introduction and Background

The following section discusses digital imaging systems, the affect of their design parameters on image quality and patient dose and conventional QC methods. Chapter 2 discusses the fundamentals of noise and NPS. In chapter 3, we describe data collection and NPS calculation. Chapter 4 will cover the results of the measurements which will be subsequently discussed in chapter 5. Finally, chapter 6 concludes the result of this work and proposes possible areas for future research.

1.2 Background

The general schematic of DR systems is shown in figure (1-1). A DR system consists of x ray generator, x ray tube, digital detector and readout electronics. In the following section, each of these components and the affect of their design parameters on the system performance will be described.

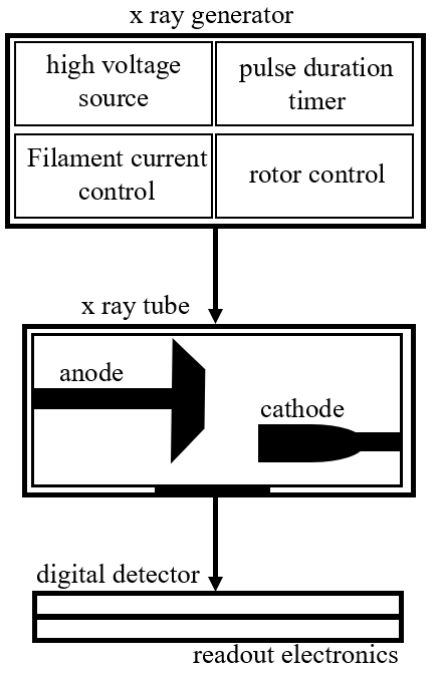

Figure 1-1. The general schematic of a digital radiography system.

1.2.1 Digital Detectors

The factor that distinguishes DR systems from conventional film-based systems arises from the last steps of imaging chain: detection, processing and representation of the image [4]. The digital detector task is to absorb x ray photons and convert them into electrical charges. Subsequently, electrical charges are recorded and digitized and then represented in gray scale. Finally, post-processing is applied on the raw data in order to obtain the most diagnostically reasonable image, and processed image will be stored at a digital archive.

Generally, digital imaging systems are categorized into two groups: computed radiography (CR) and digital radiography (DR) systems [10]. This categorization depends on the differences among these digital technologies with respect to three basic components of a digital detector: the capture, the coupling and the charge readout components [11].

CR systems use an indirect process of conversion by means of storage phosphor plates and a separate image readout procedure. DR systems are further split into direct and indirect DR. Direct DR systems use a photoconductor, mostly amorphous selenium in order to convert x ray photons into electrical charges [10].

The mechanism of indirect detectors is designed to first convert x rays into light and then, the electrical charges will be produced [11]. Indirect conversion in digital radiography are either accomplished by a CCD (charged coupled device) or a flat panel detector. The CCD x ray imaging systems are seldomly used clinically. Flat panel indirect DR systems consist of a scintillator layer, an amorphous silicon photodiode circuit and a TFT array. The scintillator array converts x ray photons into visible light, then the light will be detected by the photodiodes and electrical charges will be produced. A TFT array will readout electrical charges. The most common scintillator used in flat panel detectors are cesium iodide (CsI) and gadolinium oxisulphade (Gd_2O_2S). [11]. Indirect flat panel DR systems are the most commonly used in medical digital radiography.

Two distinct processes that take place in the capture element directly affect the spatial resolution and the noise of the system. First, the scattering, fluorescence or photoelectric effect can cause dissipation of the energy of x ray photons across the detector plane. Secondly, the scattering of the secondary particles converted from the x ray photons by the capture element can also add more blurring to the detector's response. In case of scintillator-based detectors, these secondary particles are the visible light photons which are produced through the interaction between x ray photons and

the phosphor. In case of direct digital detectors, the electronic charges are the secondary particles which are generated from the interaction of x ray photons and the photoconductor [12]. Scattering caused by the scintillator plays an important role in the spatial resolution of indirect DR detectors. Decreasing the thickness of the scintillator crystal can help reducing the blurring which, however, reduces the x ray detection efficiency and increases the image noise. Another approach to reduce the light diffusion in the capture element is to use needle-like structured phosphor crystals. This technology improves the spatial resolution and allows using thicker crystals which results in higher efficiency and less noise.

At the collection element, the pixel size is the dominant design parameter affecting spatial resolution and noise. According to the Nyquist sampling theorem, a detector with a pixel size, ν, can only represent objects with spatial frequencies higher than the cut-off frequency, $\frac{1}{2\nu}$. Therefore, the resolution of a detector's output is limited by the size of its pixel size. In addition, the efficiency of the collection element impacts the noise. One design approach which reduces noise is to match the spectral absorption of the collection element with the wavelength of the light in case of indirect detectors. Fluctuations in the readout process and the background noise in the electrical signal can also increase noise. Therefore, improving the electronics and the detector's cooling system can help in reducing noise [12].

Another approach which impacts resolution is to increase the fill factor of the pixels. Fill factor is defined as the ratio of the sensitive area to the whole area of a pixel.

1.2.2 X Ray Tube

X ray tube converts the electrical energy into characteristic and bremsstrahlung x rays and heat from electric current supplied by the x ray generator [13]. However, this process is very inefficient. Only 1% of the electric energy is converted to x ray photons and the remaining 99% is converted to heat. X ray tubes are designed to minimize the heat and maximize the production of x rays. The principle elements of a x ray tube include the cathode, anode, rotator/stator, tube envelope, tube port, cable sockets, tube housing, intrinsic filtration and collimators [9].

The cathode is composed of two filaments, typically made of tungsten, recessed within a focusing cup. When the energy is supplied, the circuit warms up the filament. In a process called "thermionic emission", the heat results in the release of electrons at a rate dependent on the

filament current and temperature. At a specific temperature, the electrons can leave the surface of the cathode. However, the electron current from cathode to anode requires a potential difference between them which is supplied by applying the tube voltage. The filament current and the tube voltage control the X ray intensity. The length of the filament in one direction, its position with respect to the focusing cup and the electron beam width in the perpendicular direction characterize the focal spot size. The short and long filaments used in the cathode correspond to small and large focal spot sizes, respectively [13].

The Anode, typically made of tungsten, is the positive electrode in the x ray tube. The anode generates x ray photons and dissipates the heat. Tungsten has a high melting point and high atomic number to maximize heat dissipation and bremsstrahlung generation. The anode surface is positioned at an angle with respect to the central ray in the x ray beam. This angle affects the tube output intensity and the effective focal spot size. The dimension of focal spot size usually varies between 0.1 mm – 0.2 mm. Most x ray imaging systems have two option for focal spot size: small for a better resolution and large for a greater intensity. Focal spot blooming refers to the increase in focal spot size which occurs at high exposure current due to repulsion of electrons in the electron beam when moving from the cathode to anode. Focal spot blooming will decrease spatial resolution of the system. Three common techniques have been recognized for focal spot size measurement: pinhole, slit and star pattern method [14].

The tube envelope contains cathode and anode. The envelope is usually made of glass. However, metal and ceramics envelopes are also used for some applications[13]. The purpose of the envelope is to provide support and electrical insulation and maintain the vacuum. The housing contains and supports all the components of the x ray tube. The lead shielding of the housing absorbs the radiation expect where the window is placed. Oil is used between the envelope and the housing to transfer the heat and maintain the electrical insulation.

The x ray generator consists of a high voltage power circuit, the stator circuit, the filament circuit, the focal spot selector and automatic exposure control (AEC) circuit. An electrical circuit provides the power used by the x ray tube to generate the x ray beam. The circuit connects the tube to the generator. The generator provides the current at a high voltage for the x ray tube using transformers. The transformers convert the city low voltage into high voltage using a process called “electromagnetic induction”. The generator also allows the operator to adjust tube voltage (kV),

tube current (mA), exposure time (s) and select the focal spot size. Any deviation in these factors directly impact the radiation output of the tube.

The x ray tube and generator design parameters characterize the basic properties of the x ray beam. Loading factors (tube voltage, tube current and exposure time) determine the beam intensity, x ray energy spectrum and HVL (half value layer. Also, x ray generation is one of the main sources of noise, since it is described statistically. Therefore, x ray tube and generator characteristics directly affect performance parameters including spatial resolution, noise and contrast.

1.2.3 Performance Parameters

Understanding performance parameters of DR systems and the factors that influence them is crucial to maintaining and optimizing image quality and to minimize radiation exposure. Different methods are available for evaluation of each of these parameters. In the following section, a description of DR systems' performance parameters and their conventional QC measurements are discussed.

1.2.3.1 Noise

The unwanted fluctuations which can influence interpretation of the image and radiologist's diagnosis is called "noise". In general, noise is divided into two categories, anatomic noise and radiographic noise [12]. The former is not related to the intrinsic features of the imaging system. It basically refers to the unwanted anatomic structures within the picture which are not of the interest of the radiologist. For example, when a chest radiography is done in order to detect lung nodules, but the rib is also projected on the image. However, the latter, radiographic noise, is related to the performance and characteristics of the DR imaging system [9]. Radiographic noise originates from four sources. The primary quantum noise arising from the Poisson distribution of the incident x ray photons, Poisson excess noise resulting from secondary quanta detected per primary quanta absorption, fixed pattern or structure noise which is due to variations in sensitivity of different parts of the detector, and additive electronic noise which comes from electronic elements of the DR systems [14]. Division of noise into these main sources is valid only when the detector response is linear [15].

Quantum noise is the stochastic variations in the spatial distribution of X ray photons in the image. It results from the Poisson statistics of the X ray beam. Furthermore, quantum noise includes two more random processes: secondary quantum noise associated with detection of

secondary quanta, and Poisson excess noise resulting from secondary quanta numbers' variations because of factors like poly-energetic x rays [16]. Generally, quantum noise can vary by the amount of exposure, pixel size, scatter radiation, etc.

Structure or fixed pattern noise results from sensitivity variations among detector's element and is proportional to the square of the signal [14]. To reduce read out time, each array of detector elements has its own readout channel. However, these channels are not always tuned with respect to each other which consequently results in this structured or fixed pattern noise in the response of digital imaging detectors. In general, structure noise results from variations in detector pixel sensitivities, non-uniformity of the detector response and dead pixels. Structure noise is one of the main sources of noise for DR detectors at high exposure. Therefore, in order to reduce this type of noise, detector-specific non-uniformity corrections like offset and gain calibrations are used. Since the magnitude and pattern on the structure noise in DR detectors may vary over time, these corrections and calibrations may be required on a regular basis.

Another type of noise in DR systems is electronic noise. Background fluctuations in electronic signals or in readout process can cause electronic noise. This additive electronic noise can also result from thermal noise, shot noise and other electronic noise sources. Electronic noise amplitude can even go higher if the electrons causing this noise are added to the signal before amplification process. Methods to reduce this type of noise include cooling of the detector to minimize thermal noise and use of improved electronics [9],[12].

Noise of a DR system can be described in terms of standard deviation of pixel values or signal-to-noise ratio (SNR). The SNR is a measure of the signal level in the presence of noise which depends on the size and the shape of the object being imaged. While such tests can be easily performed by physicists, technologists may not understand their quantitative aspect. The noise power spectrum (NPS) is another method used to understand the noise content of the image. The NPS describes the frequency-dependent response of the imaging system to the noise input [9],[17].

1.2.3.2 Spatial Resolution

Spatial resolution refers to the ability of the imaging system to distinguish fine details [12]. Spatial resolution of a DR system is determined by the focal spot size, detector technology and pixel size.

When a signal with a specific contrast at a given frequency is received by the imaging system, an output image will be produced at the same frequency usually with a reduced contrast. This reduction in contrast, which is called “blurring”, is due to the system’s spatial resolution limitations. Blurring projects a localized point into a diffused point on the image. The modulation transfer function (MTF) is the most widely accepted standard to describe and characterize sharpness of an imaging system [9]. It is defined as the absolute value ratio of the modulation contrast of output to input at a given spatial frequency.

MTF is plot of the imaging system modulation as a function of spatial frequency. A system with a higher MTF produces an output with a better resolution and contrast transfer. Spatial resolution of a system is usually assessed in terms of MTF using various methods.

1.2.3.3 Contrast

Contrast resolution refers to the level of ability of the imaging system to distinguish low contrast objects. Contrast resolution of an x ray imaging system can be described in terms of subject contrast and detector contrast. The contrast of signal intensity of the image after attenuation in the object and prior to the image processing is referred to as subject contrast. Detector contrast corresponds to the energy response and other properties of the detector like detector’s dynamic range [18],[9].

In medical imaging, contrast is described using the signal difference-to- noise ratio (SDNR). The SDNR is the difference between the signal intensity of a particular structure in the region of interest (ROI) and the signal intensity of the background with respect to the noise level of that ROI is measured, as described in the following equation,

$$SDNR = \frac{I_b - I}{\sigma_b} \tag{1-2}$$

Where I is the signal intensity of the image in the region of interest, $I_b$is the signal intensity of the background surrounding the object b and σ_b is the standard deviation of the background.

1.2.3.4 Systematic Artifacts

Various types of artifacts can appear on the output of an imaging. Therefore, it is important to include tests in the quality control program to detect different artifacts

Variations in conversion layer thickness and electronic gain and offset makes flat panel DR detectors inherently non-uniform. Differences in sensitivity and response of TFT arrays and poor coupling between the detector layers also result in artifacts in the image. These artifacts are removed by correction software [19]. Another predominant artifact related to flat panel detectors are the malfunctioned pixels referred to as “dead pixels” [20],[21]. Dead pixels may be observed on the image as cold spots, rows, columns, or clusters. In order to correct the system for this type of artifact, the pixel values are interpolated by averaging the adjacent pixels [9]. If the number of dead pixels exceeds the acceptable range or they appear as clusters covering multiple rows or columns, simple interpolation may not be sufficient. In this case, the correction of loss of data might require other interpolation techniques or even replacement of detector array.

Ghosting and lag are also artifacts associated with DR detectors [20]. Lag is the manifestation of the release of a trapped charge which increases the image signal. Ghosting is the appearance of a gain in sensitivity due to detector over-exposure [22]. If the system acquires images at a considerably fast rate, then a ghost image might appear on the subsequent image as a result of the trapped charges from the previous readout. Lag signals can be minimized by allowing time between each exposure. Therefore, it might seem that this type of artefact is not clinically significant. Nonetheless, in cases that image acquisitions must be done successively at a fast rate a ghost of previous exposures may become significant [19]. In addition, grid-related problems can also result in obscuring artifacts in different types of DR systems.

1.2.4 Conventional Quality Control Tests

Table (1-1) describes the annual quality control tests recommended by Health Canada for digital radiography. In following, the recommended QC procedures and their acceptable criteria by Health Canada safety code 35 are discussed.

Table 1-1. Recommended annual QC tests by Health Canada Safety Code 35 [1].

QC procedure	Equipment
Spatial resolution	Spatial resolution test tool (edge, slit, bar pattern)
Contrast detectability	Contrast detectability test tool, CNR
Noise, uniformity and artifacts	Sheets of uniform tissue equivalent attenuator
Accuracy of loading factors	X-ray tube voltage meter, Irradiation time meter, Current meter
Radiation output reproducibility	Dosimeter
Radiation output linearity	Dosimeter
X ray beam filtration	Dosimeter
Response function	Dosimeter, Sheets of uniform tissue equivalent attenuator
Image lag	Rotatable spoke test tool pattern
Grid performance	Sheets of uniform tissue equivalent attenuator

1.2.4.1 Assessment of Spatial Resolution

The MTF is the most common metric to measure the spatial resolution of an imaging system. There are three methods for assessment of spatial resolution of a DR system: imaging a bar pattern, slit or edge [12].

A bar pattern test object with increasing narrower dark and light patterns is used to assess the resolution of the system. This method is not a direct measure of MTF. The test object is made of a thin layer of high atomic number metals e.g. Pb which covers a range of frequencies. An image is acquired after placing bar pattern in the image, either parallel to the x or y axes, or along a 45° diagonal. Then the response amplitude at each of discrete frequencies on the bar pattern is deduced by analyzing pixel values behind the bar pattern. This response amplitude corresponds to the square wave response function of the system. The MTF is then calculated from the square wave response function [20]. Although bar pattern method is simple and fast, it is limited in precision and makes a rough estimation of frequency responses. Therefore, it is not recommended for deriving the MTF.

In the slit method, two thick pieces of metal, held at a precise distance from each other, form the slit with a width of tens of microns. The slit must be in an accurate alignment with the beam and detector. It is placed at a very small angle (1.5-3°) with respect to the pixel arrays. Then, one or more images are acquired at high exposures in order to measure the line spread function (LSF). The MTF of the system is derived from the Fourier transform of the LSF. Implementation of this method is difficult, time consuming, and requires precise alignment of the slit [23].

The edge method is a somewhat simpler method to calculate the MTF. The edge is placed at small angle with respect to the pixel arrays. The edge response function of the system is then computed by plotting the pixel values against the distance from the edge. The LSF perpendicular to the edge is calculated by taking the derivative of the edge response function. The MTF of the system is derived from Fourier transform of the LSF.

MTF methods require precise alignment and a software to analyze the results [24]. Moreover, all these methods are localized to the region of the image where the test object is placed suffer from subjectivity of the evaluation. They are typically beyond the scope of an x ray technologist or a clinical physicist. Kuhls et al have shown that the MTF can be derived from the NPS [24],[25].

1.2.4.2 Contrast, Noise, Uniformity and Artifacts

Multiple homogeneous phantoms with thicknesses representing various patient thickness are required to assess the image noise, uniformity and artifacts. According to Health Canada recommendation, SNR of the image must be calculated in order to characterize noise. In addition, standard deviation should be computed at three location of the image: the centre, the top and side.

In addition to SNR, the NPS characterizes the noise properties of the imaging system. For digital systems, NPS is calculated by a two-dimensional Fourier analysis method using homogeneous images, called flat field images [12]. As discussed earlier, in this method, image is truncated into multiple regions of interest. Then, the noise power spectra are calculated for each region and averaged to compute the 2D NPS. Finally, the 1D NPS is derived by averaging 2D NPS radially, diagonally or orthogonally [12].

Contrast detectability can also be evaluated according to the manufacturer's recommended test procedures to assure that the CNR is within manufacturer specifications. For this purpose, a phantom with different contrast levels is usually used.

1.2.4.3 Accuracy of Loading Factors

According to Health Canada Safety Code 35, for any combination of loading factors, x ray tube voltage deviation from the actual value must not exceed 10%, the loading time deviation from the actual value must not exceed (10% +1ms), x ray tube current deviation from the actual value must not exceed 20%, and the current-time product deviation from the selected value must not exceed (10% +0.2mAs). The required equipment to measure these parameters include x ray tube voltage meter, irradiation time meter and current meter [1].

1.2.4.4 Radiation Output Reproducibility and Linearity

For any combination of loading factors, the coefficient of variation of any ten consecutive exposure measurements, with the same source to detector distance and taken within a time interval of one hour, must be less than 0.05, and each of the measurements must not deviate by more than 15% of the average of the ten measurements.

Further, the quotient of the measured average kerma divided by the measured time current product acquired at two consecutive x ray tube current settings must not be larger than 0.1 times their sum.

1.2.4.6 X Ray Beam Filtration

According to Health Canada safety code 35, the measured half value layer (HVL) must not be less than the values provided by IEC (International Electrotechnical Commission). Quality control of HVL is important to measure if low energy x ray photons are removed from the beam by filtration.

1.2.4.7 Image Lag and Grid Performance

It must be assured that there is no residual image from previous exposures. For this purpose, CNR between two regions of interest from a flat field image is calculated. Prior to the flat field image acquisition, an image is acquired in which half of is the field of view is covered with an Aluminum sheet. The CNR is then calculated between the previously covered and uncovered regions, to determine if ghosting is significant.

Anti-scatter grids are used to reduce the amount of scatter in the image. A routine test check must be carried out to ensure that the grid does not introduce non-uniformities or artifacts in the image.

1.3 Research Rationale and Objective

The aim of this study is to evaluate the NPS as a system performance constancy test for DR imaging systems in a routine QC program. Computing the NPS is fast and reproducible. The NPS can be decomposed into its three components. Therefore, it may also be able to identify the sources of performance deviation in the imaging system. For this purpose, we will investigate if different types and levels of deviation in DR imaging system's performance will impact the NPS or not. In addition, by decomposing the NPS we will investigate if the change in these components reflects the cause of system performance deviation. If NPS is sensitive to system performance deviations and its components point to the possible cause, then it can be used as a constancy test for performance assessment of different aspects of the imaging system.

Chapter 2

Noise Power Spectrum

2.1 Stochastic Component of Imaging Systems

Systems can generally be categorized into two groups: deterministic and stochastic. A deterministic system is always precisely predictable. However, it is not possible to exactly predict the output of a stochastic system. An imaging system is stochastic due to stochastic fluctuations in the signal which are called noise [20] [9].

For x ray medical imaging systems, the discrete nature of energy in form of x ray photons, detected at each pixel, dominates the stochastic variations in the system. In general, multiple random processes result in variations in the output of a x ray imaging system: the number of incident x ray photons (Poisson process), the number of primary photons which are absorbed by the object of interest (Binomial process), the number of light photons generated per absorbed x ray photons (Binomial process), and the response of TFT-array to light photons (Binomial process). Since the combination of Binomial and Poisson processes results in a Poisson process, the noise distribution function in x ray imaging systems can be considered as Poisson distribution which is described by:

$$p(k) = \frac{\lambda^k e^{-k}}{k!} \qquad (2\text{-}1),$$

where $p(k)$ is the probability of incidence of k photons and λ is the average of photons per pixel. The mean and variance of a Poisson process is also λ.

2.1.1 Random Processes

A random variable, X, is a variable whose possible values are the outcomes of a random phenomenon. A distribution function, F(x), can be defined for random variable, X, which represents the probability, P, of the event of having the outcome, x, which is less than or equal to x:

$$P[X \leq x] = F(x) \tag{2-2}$$

The probability of the random variable, X, taking values between x_1 and x_2 is given by:

$$P[x_1 \leq X \leq x_2] = F(x_2) - F(x_1) = \int_{x_1}^{x_2} p(x)dx \tag{2-3}$$

where $p(x)$ is the probability density function:

$$p(x) = \frac{d}{dx}F(x) \tag{2-4}$$

$p(x)$ is always positive and its integral over the whole domain is 1. The probability density function can be of various forms such as binomial, Poisson, Gaussian, uniform, etc. [26]

Two important characteristics of a random variable are the expected value and variance. The expected value of a random variable, X, is given by:

$$E(X) = \int xp(x)dx \tag{2-5}$$

The variance, σ_x^2, is described as the expected value of the squared deviation from the expected value as given by:

$$\sigma_x^2 = E[|X - E(X)|^2] = E\{X^2\} - |E\{X\}|^2 \tag{2-6}$$

The square root of variance is called standard variation:

$$\sigma_x = [E(x^2) - \bar{x}^2]^{\frac{1}{2}} \tag{2-7}$$

Chapter 2. Noise Power Spectrum

Suppose that random variable, X, is a function of spatial dimension, u, Then the autocorrelation of $X(u)$ will be $\mathrm{R}_X(\mathrm{u}', \mathrm{u}' + \mathrm{u})$ which is describes by:

$$\mathrm{R}_X(\mathrm{u}', \mathrm{u}' + \mathrm{u}) = \mathrm{E}\{X(u')X^*(u' + u)\} \quad (2\text{-}8),$$

where * represents the complex conjugate. This equation demonstrates the correlation of $X(u')$ with itself at a displacement by u.

Similarly, the autocovariance indicates the correlation of $x(u')$ with itself at a displacement by u about the expected values. The equation for autocovariance is given by:

$$K_X(\mathrm{u}', \mathrm{u}' + \mathrm{u}) = \mathrm{E}\{(X(u') - E(X(u')))(X(u' + u) - E(X(u' + u)))\} \quad (2\text{-}9)$$

$$= \mathrm{R}_x(\mathrm{u}', \mathrm{u}' + \mathrm{u}) - \mathrm{E}\{X(u')\}\mathrm{E}\{X^*(u' + u)\} \quad (2\text{-}10)$$

A random process is an infinite indexed collection of random variables defined over a common probability space. The index parameter can be spatial dimension or time. In case of x ray imaging, a random process is any mechanism resulting in the random fluctuations in the signal.

2.1.2 Ergodic Wide-Sense Stationary (WSS) Random Processes

A random process is called wide-sense stationary (WSS) when, at least, its expected value and autocorrelation are stationary in space. For instance, if $X(u)$ in equation (2-8) is a WSS random process, then the autocorrelation will only depend on the displacement u, and the position u' will not affect it, which means that for a WSS random process, the equations for autocorrelation and autocovariance will be simplified to:

$$\mathrm{R}_X(\mathrm{u}', \mathrm{u}' + \mathrm{u}) = \mathrm{R}_X(\mathrm{u}) \quad (2\text{-}11)$$

$$K_X(\mathrm{u}', \mathrm{u}' + \mathrm{u}) = K_X(\mathrm{u}) \quad (2\text{-}12)$$

In order to characterize noise in medical images, we assume that the random process is wide-sense stationary (WSS), meaning that any shift in space does not affect the mean and covariance of the stochastic process.

In addition to wide-sense stationary assumption, the noise in medical imaging is assumed to be ergodic. This assumption simplifies the characterization of noise significantly. Ergodicity means that the expected value can be derived from spatial averages. If we assume that $K_{X,U}(u)$ is the

sample autocovariance, then $K_{X,U}(u)$ gives an estimation of the autocovariance of the WSS ergodic random process. In other words,

$$K_{X,U} = \frac{1}{U}\int_U \Big(X(u') - E\big(X(u')\big)\Big).\big(X(u'+u) - E\big(X(u'+u)\big)\big)du' \tag{2-13}$$

$$\lim_{U\to\infty} K_{X,U} = K_X(u) \tag{2-14}$$

The assumption of ergodicity results in faster and less complicated calculations. In general, the two assumptions of the random process being wide-sense stationary and ergodic are essential in order to describe image noise in the Fourier domain. The first assumption is usually met for noise analysis in low-contrast imaging. The ergodicity assumption can also be valid by applying some approximations [20].

2.1.3 Noise Power Spectrum of an Ergodic WSS Random Process

The autocovariance of an ergodic WSS random process describes the second order second moment statistics in the spatial domain. The noise power spectrum (NPS) characterizes the same properties in the frequency domain. The NPS is the Fourier transform of the autocovariance function which indicates each frequency bin's contribution to the variance. Therefore, NPS is expressed as a function of spatial frequency.

NPS of an ergodic WSS random process can be derived from the sample autocovariance when U→∞, as follows:

$$NPS_x(v) = \lim_{\mathrm{U}\to\infty} \frac{1}{U} E\left\{\left|\int_U (X(u) - E\big(X(u)\big))e^{-i2\pi uv}dv\right|^2\right\} \tag{2-15}$$

where v is the frequency variable[20].

2.2 Practical Computation of the NPS

Equation (2-15) describes the NPS of a one-dimensional ergodic WSS random process. Likewise, the NPS of a two-dimensional WSS random process $D(x,y)$ can be described as:

$$NPS_D(u,v) = \lim_{X,Y\to\infty} \frac{1}{XY} E\left\{\left|\int_X\int_Y (D(x,y) - E\big(D(x,y)\big))e^{-i2\pi(ux+vy)}dxdy\right|^2\right\} \tag{2-16}$$

$$= \lim_{X,Y\to\infty} \frac{1}{XY} E\left\{\left|F_{X,Y}\{D(x,y) - E(D(x,y))\}\right|^2\right\} \quad (2\text{-}17),$$

where $F_{X,Y}\{D(x,y) - E(D(x,y))\}$ is the Fourier transform of the zero-mean function $D(x,y) - E(D(x,y))$ over the range $\left[-\frac{X}{2}, \frac{X}{2}\right]$ and $\left[-\frac{Y}{2}, \frac{Y}{2}\right]$. The unit for the $NPS_D(u,v)$ is usually expressed as mm^2 [20].

To compute the NPS numerically, the following formula is used[20],

$$NPS(u_n, v_k) = \lim_{N_x,N_y,M\to\infty} \frac{\Delta x \Delta y}{M.N_x.N_y} \sum_{m=1}^{M} \left| \sum_{i=1}^{N_x} \sum_{j=1}^{N_y} [D(x_i, y_j) - \bar{D}(x_i, y_j)] e^{-2\pi i(u_n x_i + v_k y_j)} \right|^2 \quad (2\text{-}18),$$

where Δx and Δy are the pixel width in the horizontal and vertical directions, M is the number of ROIs and N_x and N_y are the pixel size of the ROIs in the horizontal and vertical direction. $D(x_i, y_j)$ is the signal amplitude at each location (x_i, y_j) and $\bar{D}(x_i, y_j)$ is the average signal value.

Measuring NPS does not require any test object and is accomplished by applying the above equation to uniform images. According to the IEC, to compute NPS, a square area of 125 mm × 125 mm which is located in the center of the image is recommended to be used. ROI's with 256 × 256 pixels in size are selected. These ROI's must overlap by 128 pixels in each direction. Starting at the upper left corner, the ROI's sweep through the image at 128 pixels intervals in both directions, as shown in figure (2-1). In order to compute one-dimensional NPS, the IEC recommends using 15 rows or columns of the 2D noise power spectra [27].

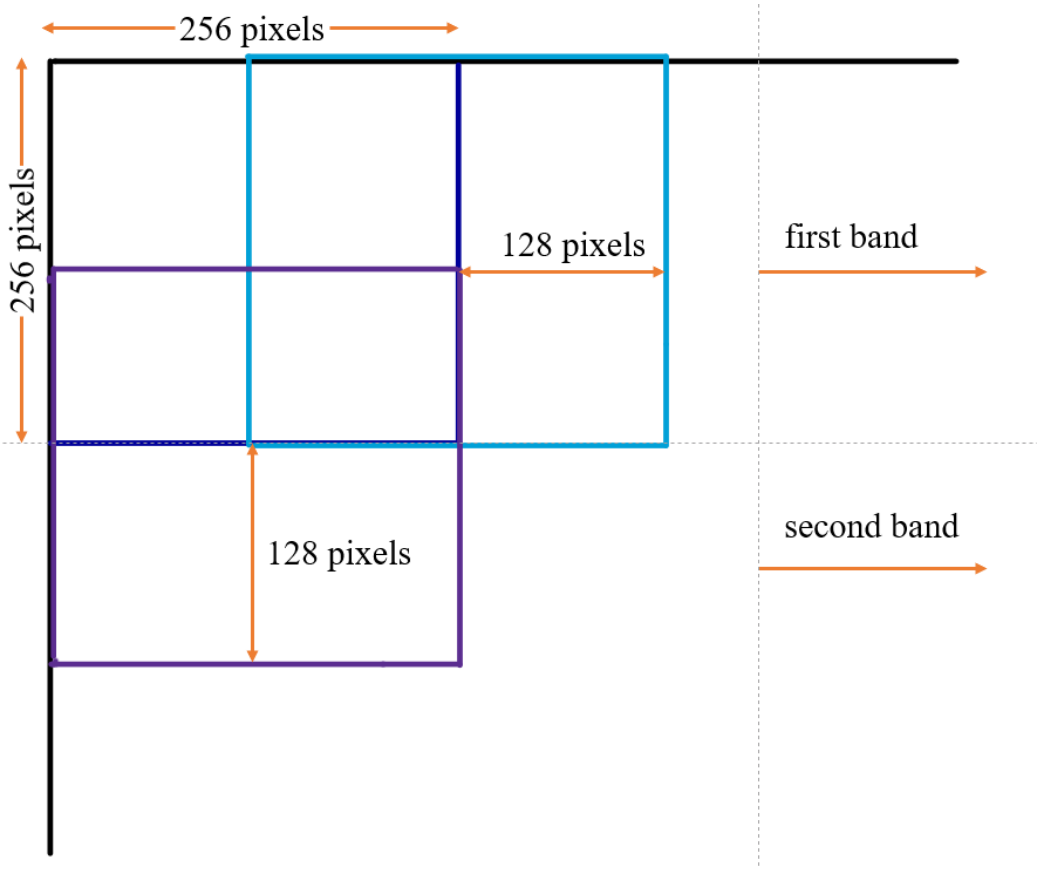

Figure 2-1. Schematic of the ROIs arrangement.

It is possible that the measurement area contains some gross exposure variations (from example, from the heel effect). In this case, normalizing the NPS can cancel some of the NPS variations due to the gross exposure. For calculation of the normalized NPS (NNPS), the NPS is normalized by the image large area signal:

$$NNPS(u,v) = \frac{NPS(u,v)}{(large\ area\ signal)^2} \tag{2-19}$$

The unit of the NNPS is area, usually mm^2 [20].

2.3 The NPS components

If the three components of noise are uncorrelated, then their respective variances can be summed up to give the variance of the total noise [28]:

$$S^2 = S_e^2 + S_q^2 + S_{fp}^2 \tag{2-20}$$

where S_e^2, S_q^2, and S_{fp}^2 are variances for each frequency bin corresponding to electronic, quantum and fixed pattern noise. Image noise can also be described as a function of image pixel value using a second order polynomial model [15].

$$S^2 = c_1^2 + c_2^2\, p + c_3^2\, p^2 \qquad (2\text{-}21)$$

where p is the image pixel value and c_1, c_2 and c_3 are the coefficients of the polynomial fitting model.

Accordingly, a three parameter polynomial curve can also be fitted to the 1D NPS and the fit coefficients at each frequency bin will represent the noise coefficient spectrum for each components of noise [29]:

$$NPS(f, D) = NPS_e(f) + NPS_q(f).D + NPS_{fp}(f)\,.D^2 \qquad (2\text{-}22)$$

where D is exposure and $NPS_e(f)$, $NPS_q(f)$ and $NPS_{fp}(f)$ are the electronic, quantum and fixed pattern noise power spectrum coefficients, respectively, which are fitted for each frequency bin. Moreover, According to Kuhls et al studies, the MTF can be derived from decomposing the NPS since the quantum NPS component is proportional to the square of the MTF [25] [26].

Chapter 3 describes methods and materials used to verify the linearity of the detector's response and the ergodicity and stationarity assumptions and to evaluate the NPS as a QC constancy test for DR systems.

Chapter 3

Materials and Methods

To investigate the use of the NPS as a system constancy test, we acquired a series of images under a variety of conditions, for which the NPS was computed. The validity of the assumptions was verified prior to the NPS calculations. The NPS was also decomposed into its components in order to determine if the change in the NPS components reflected the expected change in the quantum, fixed pattern or electronic noise components.

3.1 Image acquisition

X ray images were collected from two x ray units described in table (3-1). Uniform images, stored as "RAW" DICOM data, were selected for noise measurements. The accuracy of loading factors of the x ray tube and reproducibility of its radiation output were checked using a calibrated dosimeter (Radcal Accugold solid state detector) as shown in figure (3-1). The meter was placed at the center of the field of view. The source to image distance was set to 100 cm and the detector was positioned to cover all area of field of view.

A limited dataset was obtained using the Siemens Luminos due to clinical access issues. The extended investigation of the NPS and its decomposition was accomplished using the dataset acquired from the GE Definium.

Table 3-1. Basic technical information for the systems used for image acquisition.

System's name	Technology	Scintillator composition	Pixel spacing (mm)	Pixel matrix	Response curve
GE Definium	DR	CsI	0.19	2022×2022	Linear
Siemens Luminos	DR	CsI	0.15	2820×2820	Linear

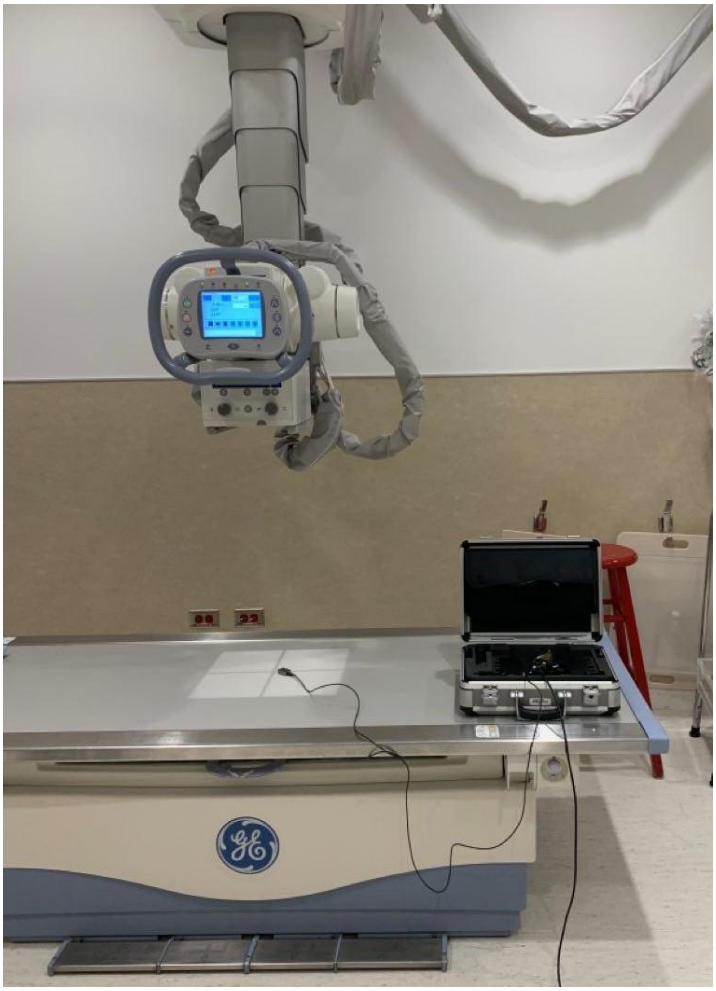

Figure 3-1. The setup used for measurement of accuracy of tube voltage, time-current product and exposure.

3.2 Linearity of Detector Response

In order to verify the linearity of the response function of detectors used in this study, the mean pixel values were measured at multiple levels of exposure. After plotting the mean pixel values versus exposure, a curve was fitted to evaluate the linearity of the detector response function for each unit. In case of the Siemens Luminos, one uniform image was acquired at each exposure level. For the GE Definium, five uniform images were averaged at each exposure level spanning the detector's dynamic range.

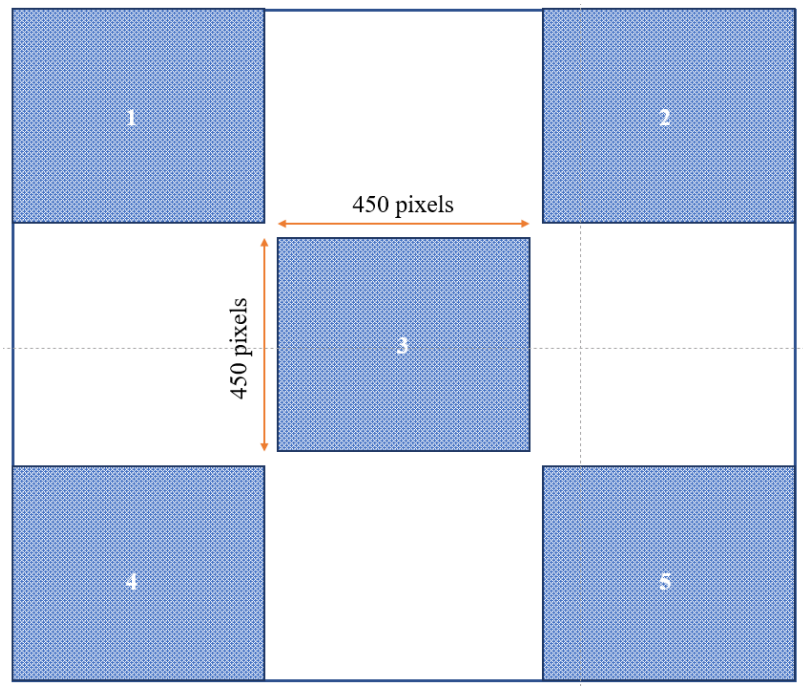

Figure 3-2. 450×450-pixel ROIs selected at upper and lower left side, upper and lower right side and center of the image.

3.3 Noise Stationarity

The normalized NPS was computed and compared for multiple ROIs at different locations in the image. As shown in figure (3-2), five ROIs with a size of 450×450-pixel were selected at the following locations: upper and lower left side, upper and lower right side and center of the image. The normalized NPS was then calculated for each of these ROI's and compared to each other. Also, the image was divided into 10×10-pixel ROI's. The standard deviations of each of these ROIs were calculated and normalized by the standard deviation calculated in the ROI at the center of the image to create a standard deviation map across the image. The stationarity assumption was investigated for both the GE Definium and Siemens Luminus system.

3.4 Noise Ergodicity

An ensemble of 50 images were used. The spatial average of a single image was compared to the ensemble average of 50 images. The average of 50 central 64×64-pixels ROI, selected on all the images of the acquired ensemble, was calculated. To calculate the spatial average for a single image, 25 ROIs of the same size were averaged. These ROIs were selected at the center of the image by moving in three different directions (horizontal, vertical and diagonal). These spatial

averages were compared to the ensemble average by computing the absolute error percentage between them. The absolute error percentage was calculated using the following equation:

$$Absolute\ error\ percentage\ = \frac{\bar{I}_{spatial} - \bar{I}_{ensemble}}{\bar{I}_{ensemble}} \times 100 \quad (3\text{-}1),$$

where $\bar{I}_{spatial}$ is the spatial average and $\bar{I}_{ensemble}$ is the ensemble average. Due to the limited availability of the Siemens unit, the ergodicity assumption was only verified for the GE Definium unit.

3.5 NPS Calculations

Computation of the NPS from uniform images was performed by developing a MATLAB code. The mean signal value can be approximated by a two dimensional polynomial fit [27], [30]. Therefore, equation (2-18) can be rewritten as:

$$NPS(u_n, v_k) = \lim_{N_x, N_y, M \to \infty} \frac{\Delta x \Delta y}{M.N_x.N_y} \sum_{m=1}^{M} \left| \sum_{i=1}^{N_x} \sum_{j=1}^{N_y} \left[I(x_i, y_j) - S(x_i, y_j) \right] e^{-2\pi i (u_n x_i + v_k y_j)} \right|^2 \quad (3\text{-}2),$$

where $S(x_i, y_j)$ is the fitted two-dimensional polynomial of the signal. A quadratic polynomial fit model is used to remove the trend the image in order to study the behavior of the stochastic component of the system. The NNPS was calculated using 128×128 ROIs which were overlapping by 64 pixels. The number of ROIs was set to be the maximum possible number with respect to the size of the image. Finally, 1D NNPS was derived from 2D NNPS by radially averaging over 7 frequency bins on either side of the NNPS axes.

The validity of the polynomial model was verified prior to NNPS calculations. For this purpose, the NNPS was computed using two methods to detrend the noise. The first method, referred to as "polynomial method", used the polynomial fit model shown in equation (3-2) to detrend the noise. The second method, referred to as "average method", used an averaged signal value of 45 repeated images (70 kV, 2 mAs). Then the Resultant NNPS of these two methods were compared to each other. In addition, the reproducibility of the results was assessed for both systems used in this study.

The acquired dataset was manipulated to mimic various types of performance deviation. Then, the NNPS was calculated for each case. To compare resultant NNPS calculations, the relative difference between two NNPS was summed over all frequencies which will be referred to as the total relative difference (TRD) in this study. TRD was reasonably sensitive to small changes and calculated the absolute difference for each point independently. TRD is calculated as the following equation,

$$TRD = \sum_{i=1}^{n} \frac{|NPS_1(i) - NPS_2(i)|}{NPS_2(i)} \quad (3\text{-}3)$$

3.6 Data Preparation

Various forms of performance deviations were introduced. These include changes in focal spot blooming, resolution, tube voltage, defective pixel artifact, image lag and mismatched grid.

3.6.1 Focal Spot Blooming

Uniform images were acquired at low and high tube current values. The high tube current values induce focal spot blooming. The properties of two images collected for this experiment are described in table (3-2).

The pinhole method was used in order to observe and measure the increase in focal spot size [31]. The setup is shown in figure (3-3) and figure (3-4). The setup consists of a pinhole assembly and a focal spot test stand, with small and large adapter rings and fluorescent screen. The resulted image of the pinhole assembly is shown in figure (3-5). Uniform images were acquired at the high and low tube current values to compute the NNPS of the images and investigate the potential impact of focal spot blooming on the NNPS.

Table 3-2. properties of images collected to observe focal spot blooming.

Image No.	kV	mAs	mA	ms	System
I	70	3.2	322	10	GE Definium
II	70	3.2	10	320	GE Definium

Figure 3-3. Focal spot test stand on table.

Figure 3-4. The pinhole assembly.

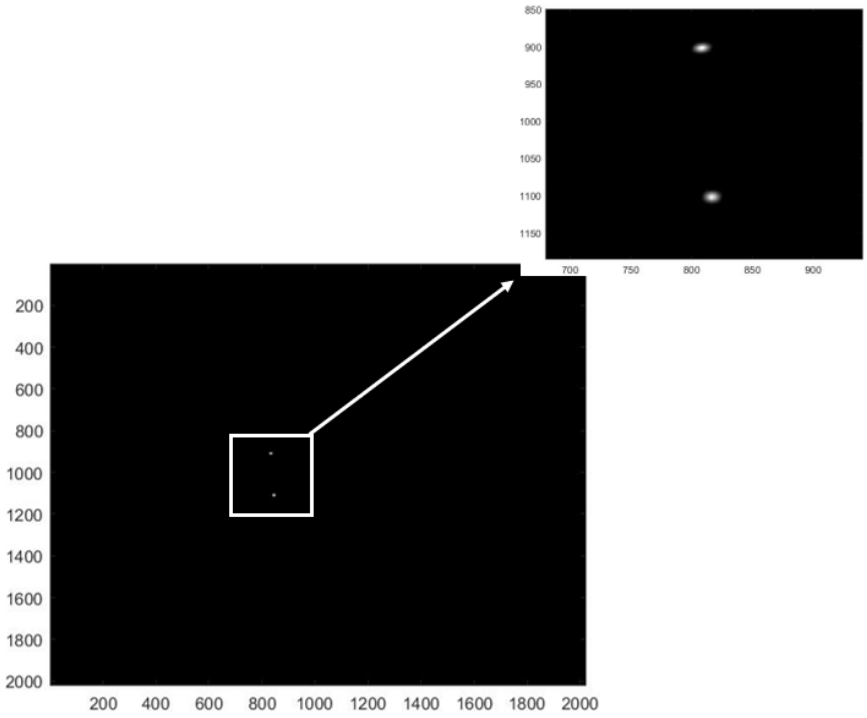

Figure 3-5. The image acquired of the pinhole assembly.

3.6.2 Resolution

In order to mimic resolution change, uniform images were collected using the large and small focal spots on the GE Definium and Siemens Luminos units. For GE Definium, the images were acquired at 70 kV and 80 kV. For Siemens Luminos, the images were acquired at 70 kV. The current-time product for all the images was 1 mAs.

3.6.3 Tube Voltage

Ten uniform images were acquired over the tube voltage range [75-85] kV and [65-69] kV in 1 kV increment. The NNPS of these images were then compared using TRD metric.

3.6.4 Defective Pixel Artifact

Defective pixel clusters were added to uniform images acquired from the GE Definium in a random fashion. The percentage of the defective pixels, their location and clustering and their values were randomized. The values of the defective pixels were set as a deviation from the image mean as follows:

$$I(i,j) = \bar{I} - k.\sigma; \qquad (3\text{-}4),$$

where $I(i,j)$ is the defective pixel value, $\bar{I}$ is the mean signal value of the image, σ is the standard deviation of the image and k is a random number between 1 and 5.

The mean squared error (MSE) was used to quantify the difference between the original image and the one where defective pixels were introduced [32]:

$$MSE = \frac{1}{n}\sum_{i,j=1}^{n}(I_{i,j} - \hat{I}_{i,j})^2 \quad (3\text{-}5),$$

where n is the number of pixels, $I_{i,j}$ and $\hat{I}_{i,j}$ are pixel values of the original and defective images.

In case of the Siemens Luminos unit, the flat panel detector had an observable fixed pattern artifact. The NNPS of the part of the image with the fixed pattern defect was compared to the NNPS of another part of the image of the same size that did not include the artifact.

3.6.4 Residual Image

A 0.51 mm thick aluminum sheet was used as the high contrast image object. As shows in figure (3-6), an image of aluminum sheet placed at the center of the field of view to the bottom was acquired using the GE Definium system.

A series of uniform images were collected after acquiring the image of the aluminum sheet. At 5, 10, 30, 60, 90 and 120 seconds after the original exposure. Two symmetric regions of interests on the flatfield image, one from the area covered by aluminum sheet and one from the background, were selected and the SDNR was calculated according to:

$$SDNR = \frac{ROI_A - ROI_B}{\sigma_B} \quad (3\text{-}6),$$

where $ROI_A$the region of interest from the area is covered by aluminum sheet, ROI_B is the region of interest from background and σ_B is the standard deviation of the background. The NNPS of the uniform images Acquired at different delay times was then computed.

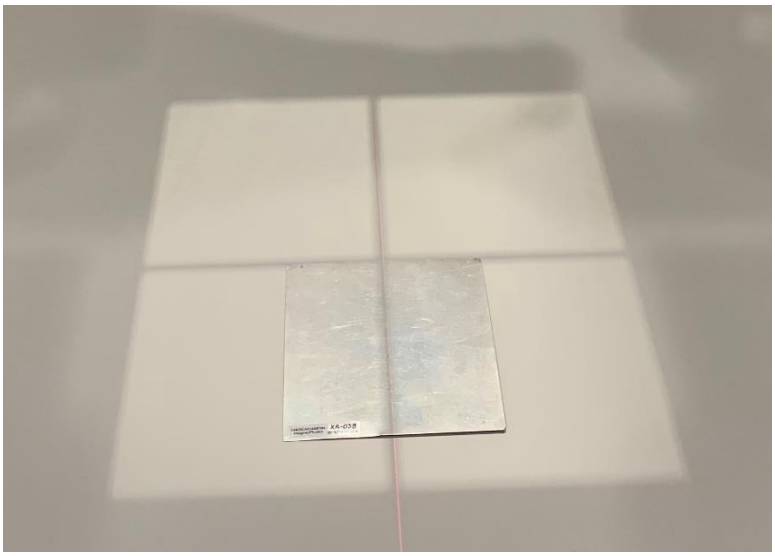

Figure 3-6. Position of the Al sheet in the field of view.

3.6.5 Mismatched Grid

A grid with the focal distance mismatched with respect to the source to image distance was placed in the grid slot above the digital detector of the GE Definium system. Uniform images were acquired at (70 kV, 3.2 mAs) and (70 kV, 5 mAs). The NNPS of the image with the grid in was compared to the NNPS of its counterpart with the mismatched grid out.

3.7 NPS Decomposition

The NPS was decomposed into three components according to equation (2-22). Electronic noise was expected to be unreliable because the imaging system used in this study would automatically correct the output for dark current. Therefore, to check the effect of excluding the electronic component of the decomposition, the NPS was also decomposed into two components using:

$$NPS(f, D) = NPS_q(f).D + NPS_{fp}(f).D^2 \quad (3\text{-}7),$$

All decompositions were performed for images acquired at 80 kV using the GE Definium unit.

In order to reduce the uncertainty of the noise coefficients estimation, the NPS was computed for multiple exposure levels over the detector's dynamic range. The coefficients were then fitted to the equation (2-24) using the $fmincon$ optimization routine. The $fmincon$ function in Matlab

calculates the minimum of a constrained multivariable function. The $fmincon$ function was used to find the minimum of the MSE function:

$$MSE = \frac{(NPS_{polynomial} - NPS_{original})^2}{length\ (NPS_{original})} \tag{3-8}$$

where $NPS_{polynomial}$ is the NPS derived from equation (3-6) and $NPS_{original}$ is the NPS calculated using equation (3-2). This method finds the coefficient at each frequency bin so that the difference between $NPS_{polynomial}$ and $NPS_{original}$ is minimum.

A measure of the accuracy of the fit was made to verify the model. For this purpose, NPS was reconstructed from its fit coefficients at different levels of exposure and was compared to the original NPS calculated by the original method.

The NPS decomposition was performed for two sets of images acquired at 75 kV and 72 kV in order to investigate the effect of tube voltage change, two sets of images acquired with small and large focal spot at 80 kV, two sets of images with and without 0.01% defective pixels at 75 kV, and two sets of images with and without the mismatched grid at 75 kV.

Chapter 4

Results

4.1 Linearity of Detector Response Function

Figure (4-1) shows the linearity of the response function of the Siemens detector for two tube voltage values. The response function of the GE Definium system is shown in figure (4-2) and the coefficient of variation (COV) in table (4-1).

The results of the response curve fitting are listed in table (4-2). The R^2 value measured for both detectors is very close to 1.

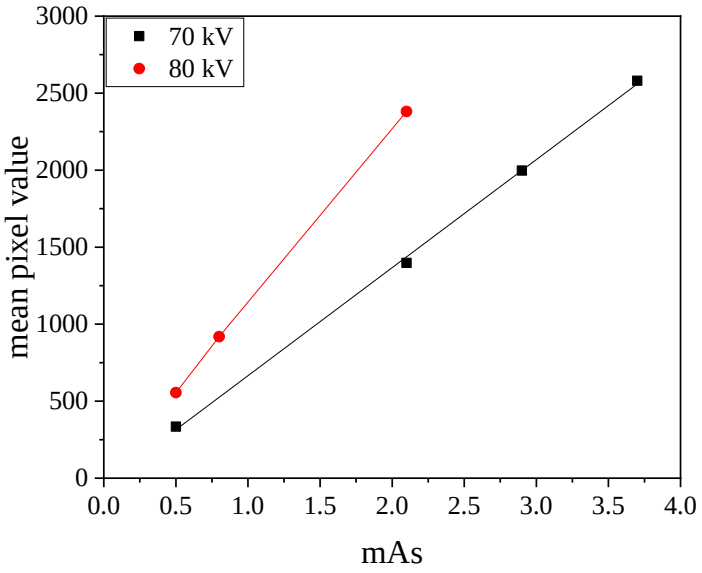

Figure 4-1. Linear response of the Siemens Luminos system at 70 and 80 kV.

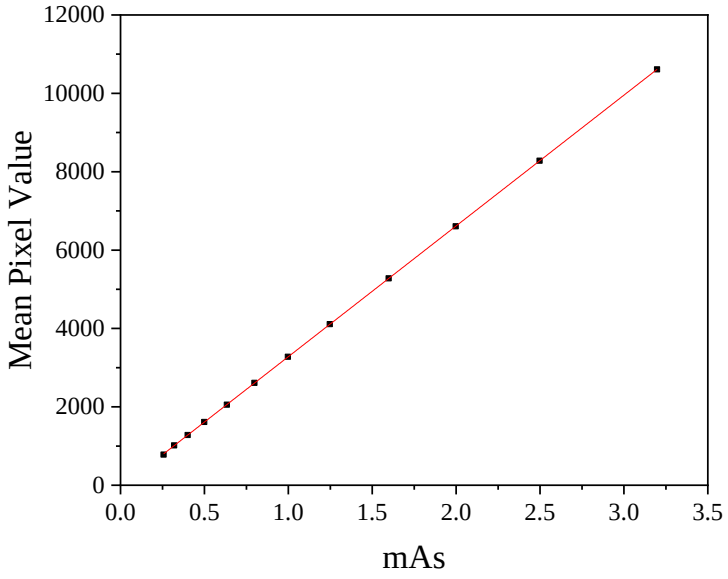

Figure 4-2. Linear response of the GE Definium system at 70 kV.

Table 4-1. The COV of the measured mean pixel values at each exposure level acquired at 70 kV from GE definium unit.

Exposure level (mAs)	COV $(\frac{\sigma}{M}) \times 100$
0.26	0.16
0.32	0.12
0.40	0.04
0.50	0.21
0.63	0.54
0.80	0.39
1.00	0.59
1.25	0.39
1.60	0.25
2.00	0.12
2.50	0.15
3.20	0.06

Table 4-2. Linear fit to detector response.

System's name	tube voltage (kV)	R-squared	Intercept	Slope
Siemens Luminos	70	0.99871	-36.1 ± 37.7	701 ± 15
Siemens Luminos	80	0.99987	-2.8 ± 17.5	1136 ± 13
GE Definium	70	0.99999	-56 ± 3	3336 ± 2

4.2 Noise Stationarity

Figure (4-3) shows the NNPS of the 450×450-pixel ROIs at different locations on the image plane. In case of the GE Definium unit, the maximum TRD was 0.38. For the Siemens Luminos unit, the maximum TRD was 2.46 in this case which appeared to be the difference between the upper left ROI and the upper right ROI. Figure (4-4) shows the calculated standard deviation map for both systems used in this study. It can be seen that the noise is not constant over the image and the periphery of the image shows higher standard deviations, particularly in case of the Siemens Luminos system. The standard deviation of all the ROIs was within 20% of the standard deviation of the central ROI except one ROI for the GE definium and two ROIs for the Siemens Luminos. The maximum difference was 25% and 32% for GE Definium and Siemens Luminos, respectively.

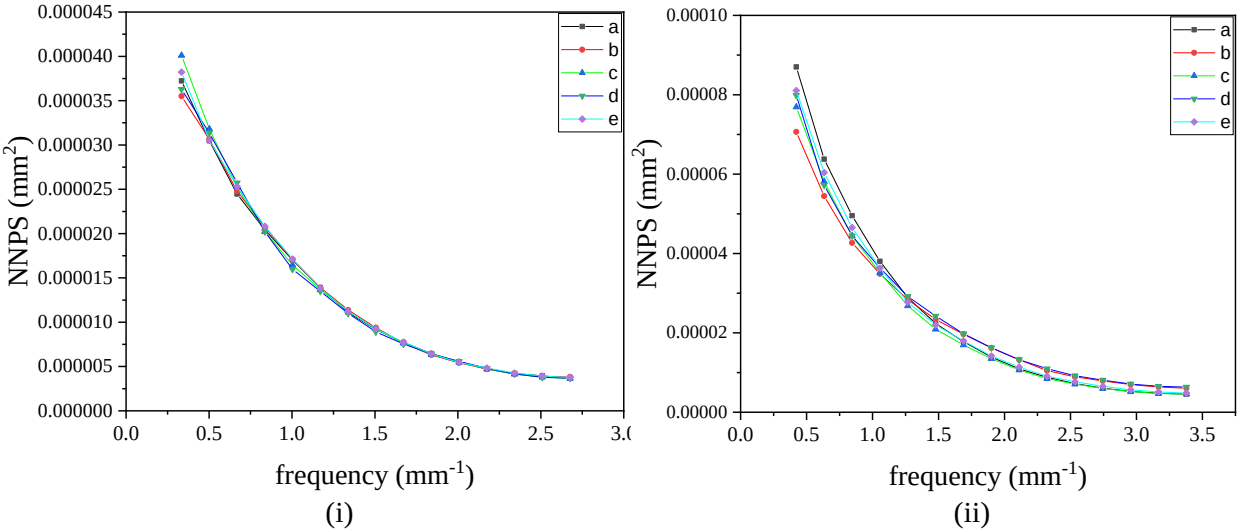

Figure 4-3. The NNPS measured for the ROIs at different locations: a) upper left, b) upper right, c) lower left, d) lower right and e) center of the image. (i) GE Definium, (ii) Siemens Luminos.

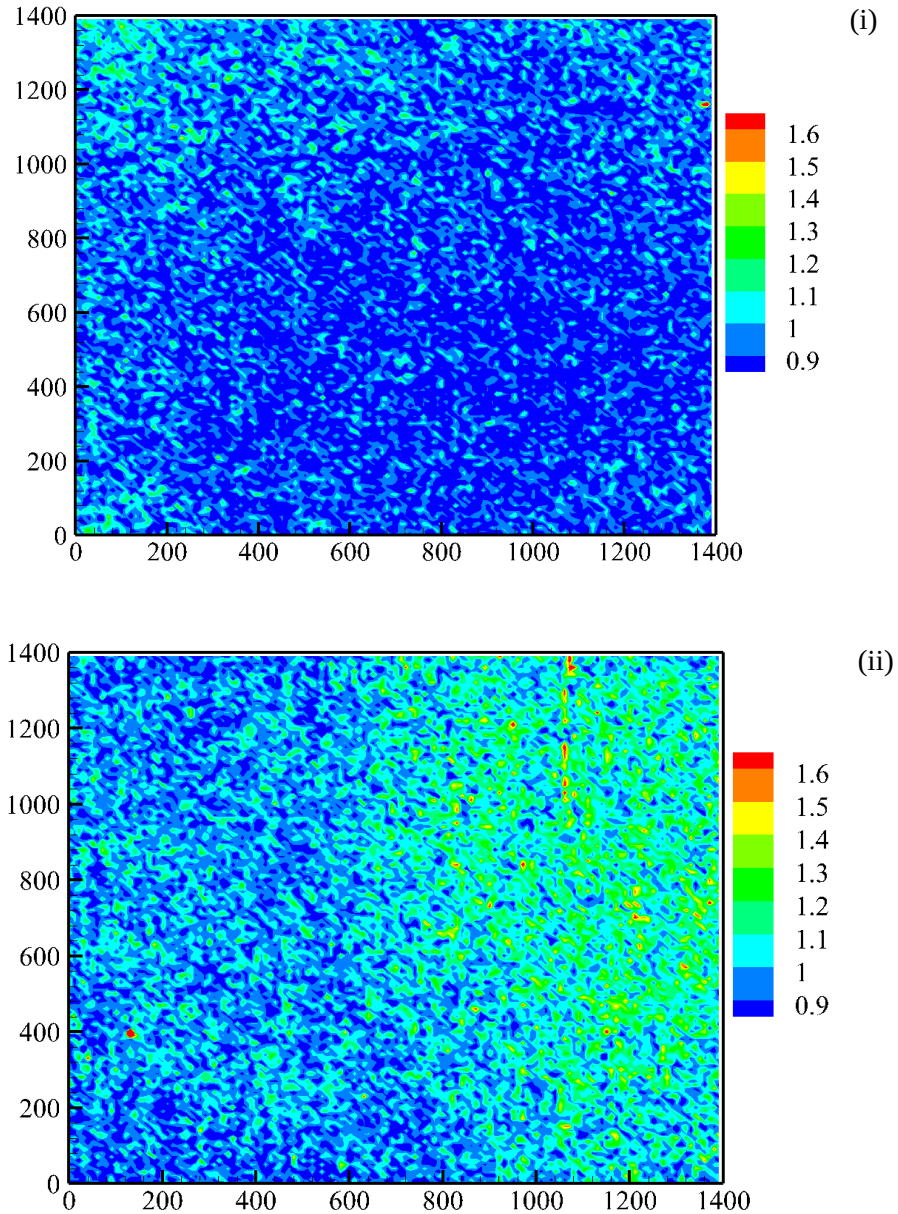

Figure 4-4. Normalized standard deviation map of the image plane using 10×10-pixel ROIs. The reference standard deviation from the central 10×10-pixel ROIs. (i) GE Definium, (ii) Siemens Luminos.

4.3 Noise Ergodicity

The absolute error percentage between the spatial average and the ensemble average is shown in figure (4-5). The maximum of absolute error between the spatial average and the ensemble average was 2.4%.

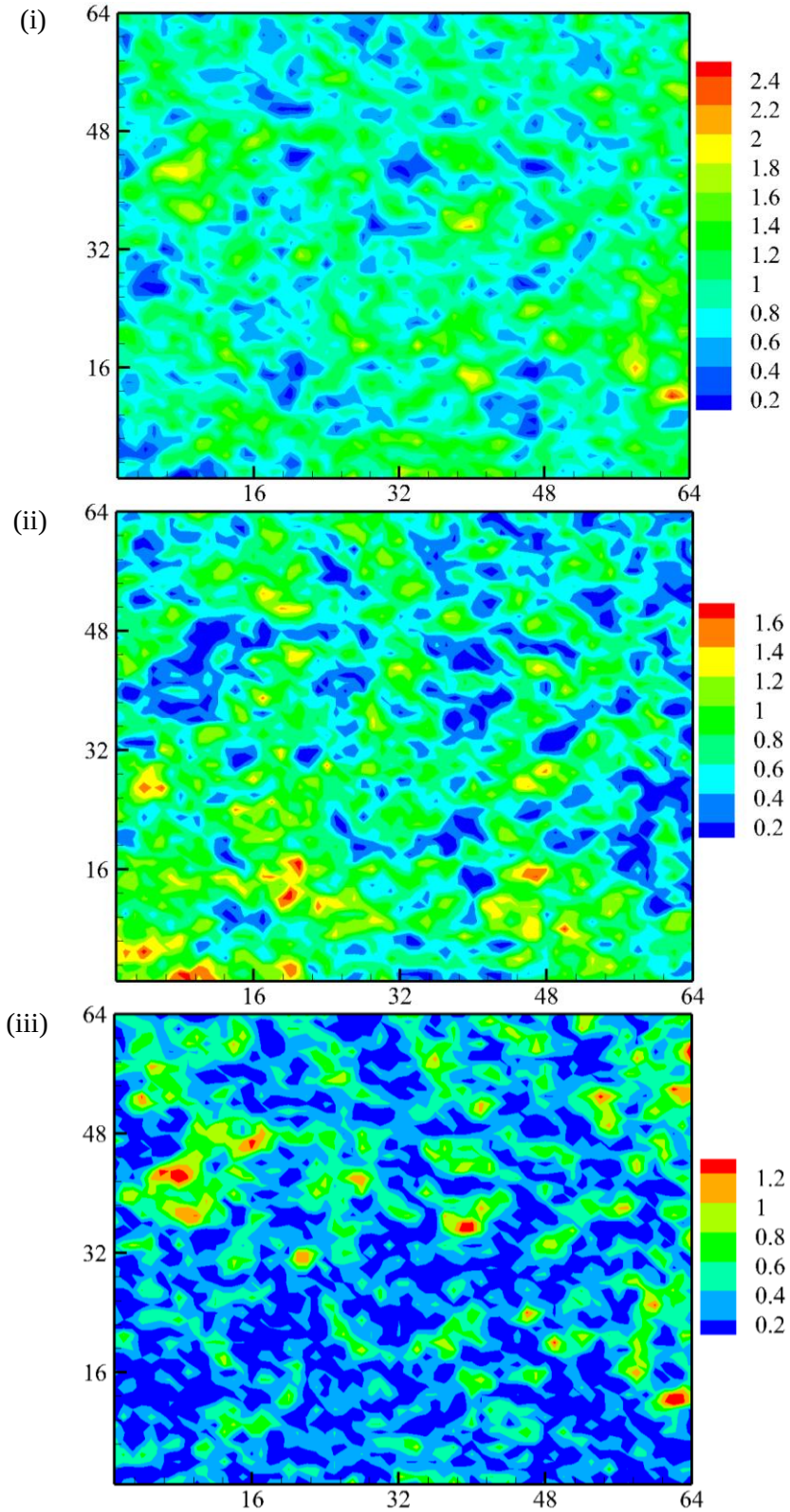

Figure 4-5. The absolute error percentage (%) map between the ensemble average and the spatial average in: (i) horizontal, (ii) vertical and (iii) diagonal direction.

4.4 Evaluation of the Polynomial Model

The accuracy of the quadratic polynomial fit used to compute the 2D NNPS was assessed prior to noise measurements. In figure (4-6), two images are illustrated: 1) the image of the polynomial fit used to detrend the noise, 2) the resultant image of noise after subtracting the polynomial fit from the signal. The NNPS calculated using the polynomial model to detrend the image is compared to the one which is detrended using the average of 45 images. As shown in figure (4-7), the noise power spectra are virtually indistinguishable. In addition, the magnitude of the TRD between these two graphs is 6.8×10^{-4}.

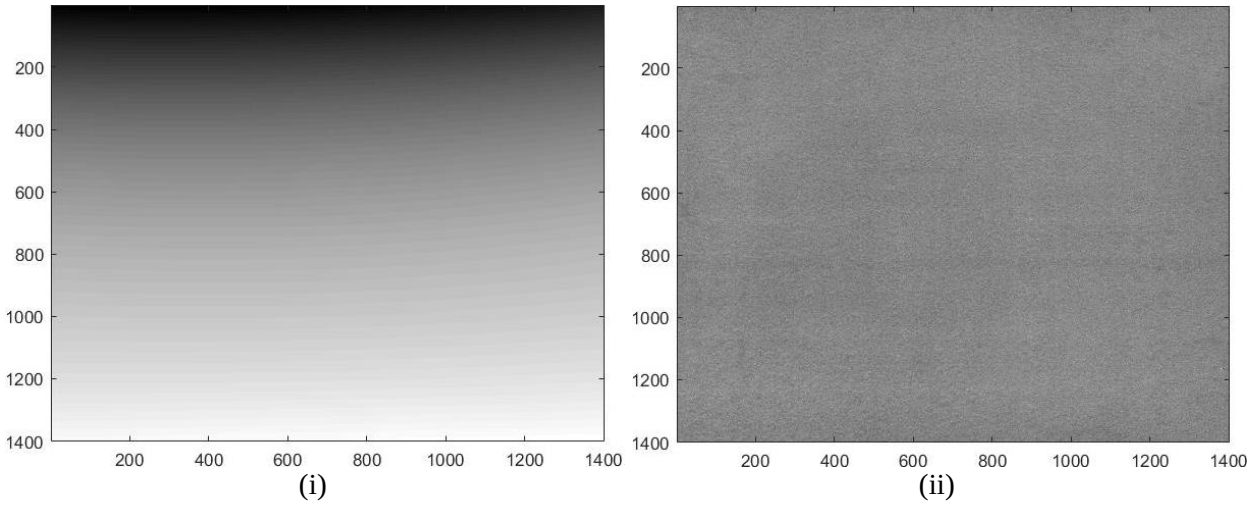

Figure 4-6. (i) the image of the polynomial fit, (ii) the noise image after subtracting the polynomial fit from signal.

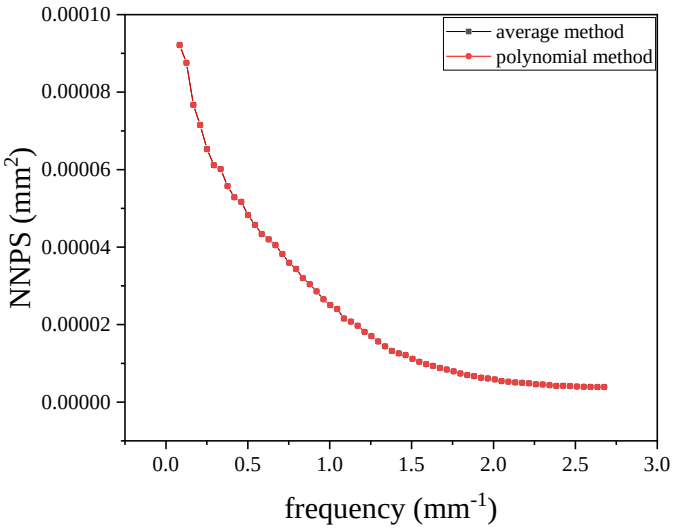

Figure 4-7. The NNPS calculated using the polynomial model and the average of 45 images.

4.5 Reproducibility of the Results

Figure (4-8) shows the calculated NNPS for the repeated image acquisitions on each of the systems. The maximum TRD for each of x ray units was then derived. The value of maximum TRD was 1.75, for the Siemens Luminos, and 0.7, for the GE Definium.

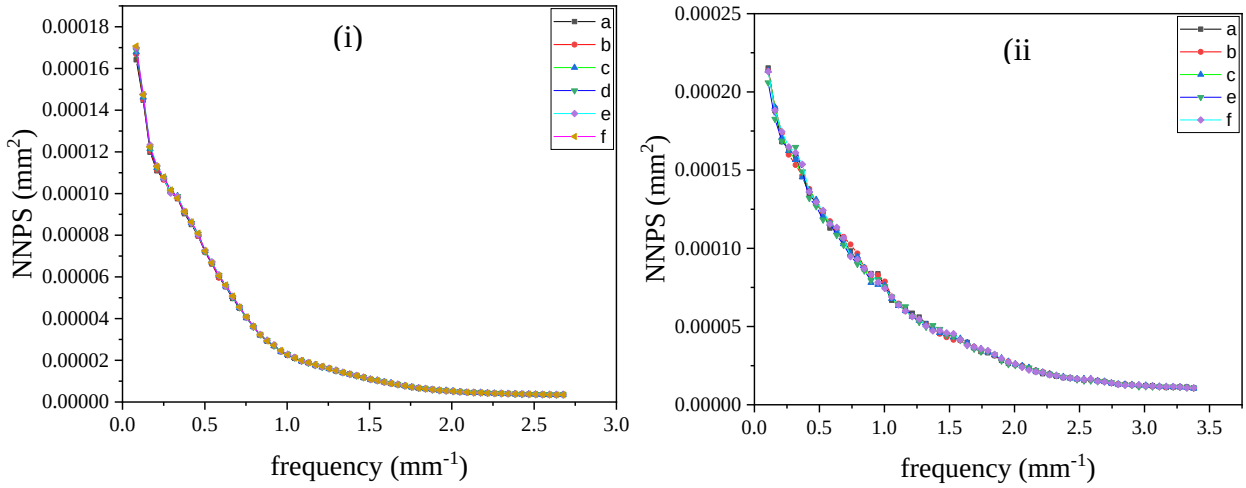

Figure 4-8. The calculated normalized NPS for six uniform images with the same loading factor values (70 kV, 3.2 mAs). (i) GE Definium, (ii) Siemens Luminos.

4.6 Focal Spot Blooming

In figure (4-9), two focal spot sizes are shown. When using a higher current value, the image of the focal spot was enlarged by 0.43 mm^2, suggesting that focal spot blooming has occurred.

In figure (4-10), the NNPS of two images acquired before and after focal spot blooming are plotted and compared. The resultant NNPS collapse on top of each other and the measured TRD between them is 0.58.

4.7 Resolution

Figures (4-11) and (4-12) show the normalized NPS between the images with small and large focal spot sizes for Siemens Luminos and GE Definium units. The TRD for each of the plots is listed in table (4-4). The NNPS of the image acquired with the small focal spot is higher than the other one. This is in agreement with the fact that a smaller focal spot results in a less blurry image and consequently, a higher MTF. The quantum noise is directly related to the square of the MTF[24]. Higher MTF means an increase in the quantum component of the noise and accordingly, a higher NPS.

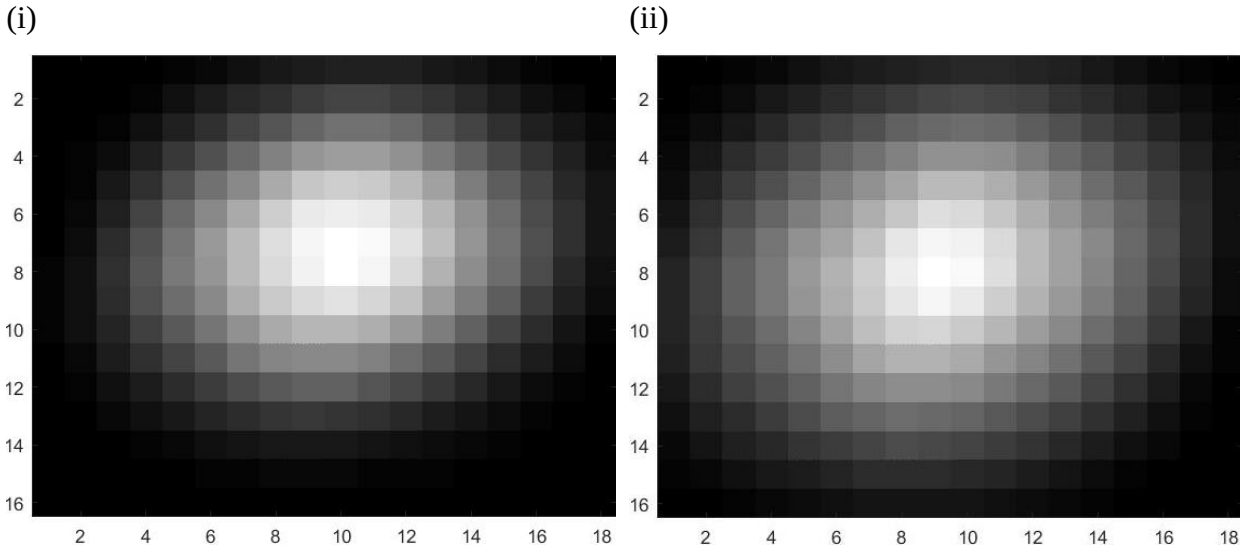

Figure 4-9. Cropped and zoomed image of the pinhole for (i) 10 mA and (ii) 322 mA. (Data: GE Definium)

Table 4-3. The loading factors used to observe focal spot blooming

kV	mAs	mA	ms	pinhole size (mm^2)
70	3.2	322	10	1.95
70	3.2	10	320	1.52

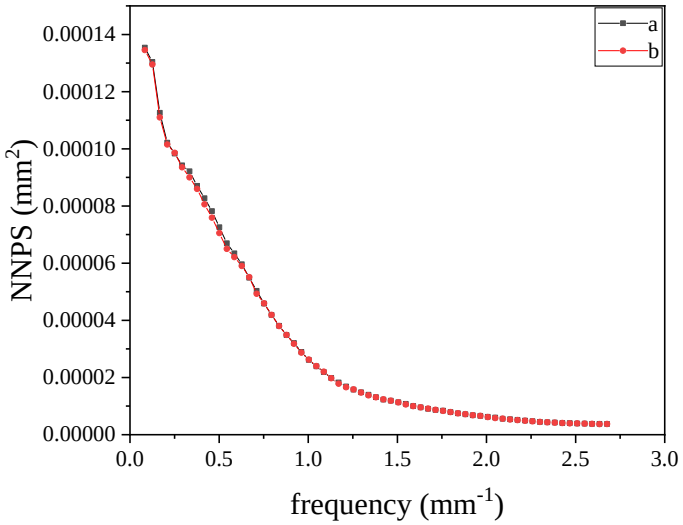

Figure 4-10. The normalized NPS for a) 322 mA and b) 10 mA. (Data: GE Definium)

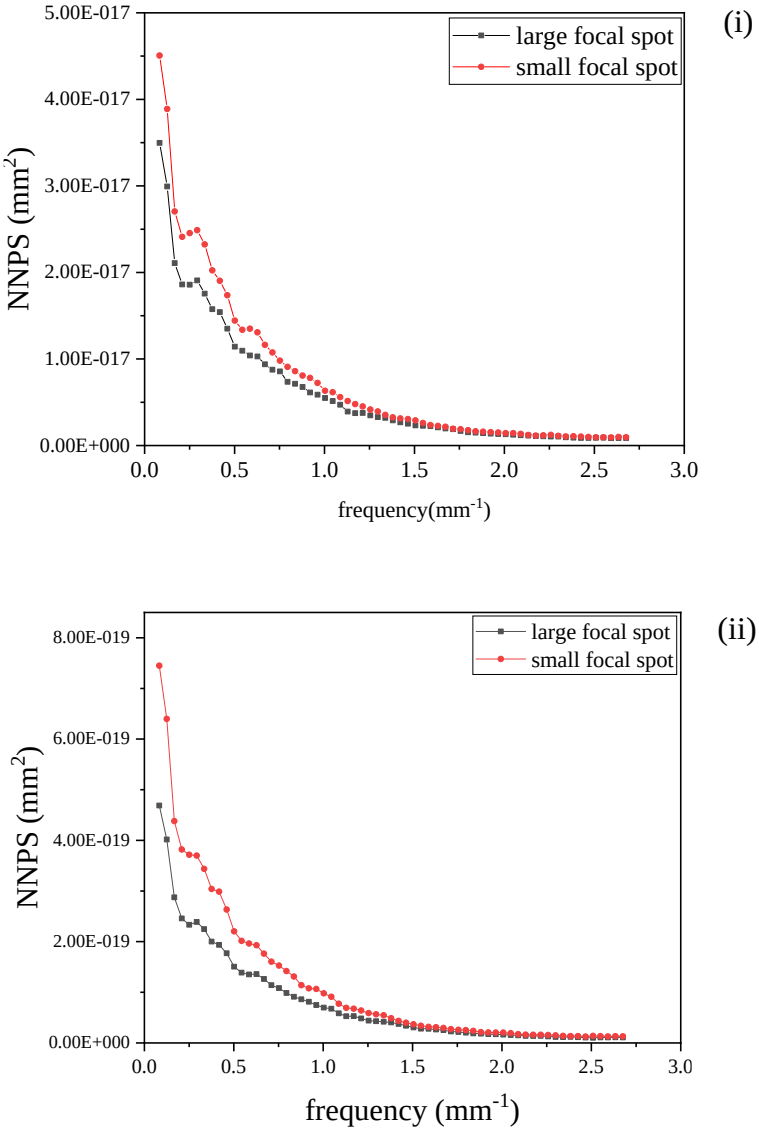

Figure 4-11. Resolution change effect on the NNPS at i) 70 kV & (ii) 80 kV for GE Definium.

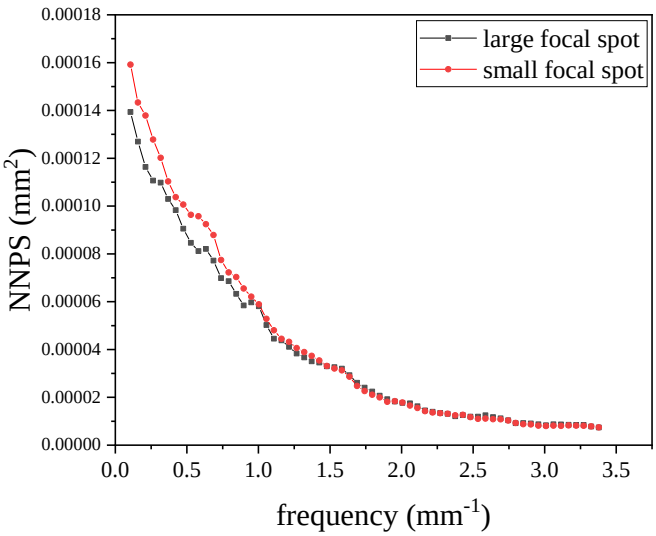

Figure 4-12. The focal spot size effect on the NNPS at 70 kV for Siemens Luminos.

Table 4-4. Comparison of NNPS between images with large and small focal spot, shown in Figure 4-12.

index	System	Voltage (kV)	mAs	TRD
i	GE Definium	70	1	1.0
ii	GE Definium	80	1	1.4
iii	Siemens Luminos	70	1	3.3

4.8 Tube Voltage

Results from figure (4-13) show that the NNPS decreases when the tube voltage increases. A1 kV tube voltage deviation from 80 kV resulted in a TRD equal to 1.80. As the shift in tube voltage value gets larger, the difference between the NNPS also rises. When the nominal kV is 65, a deviation as low as 2 kV produces a TRD equal to 3.3. The TRD between the NNPS for the image at the nominal value and the images at different levels of deviation from the nominal value is shown in figure (4-14).

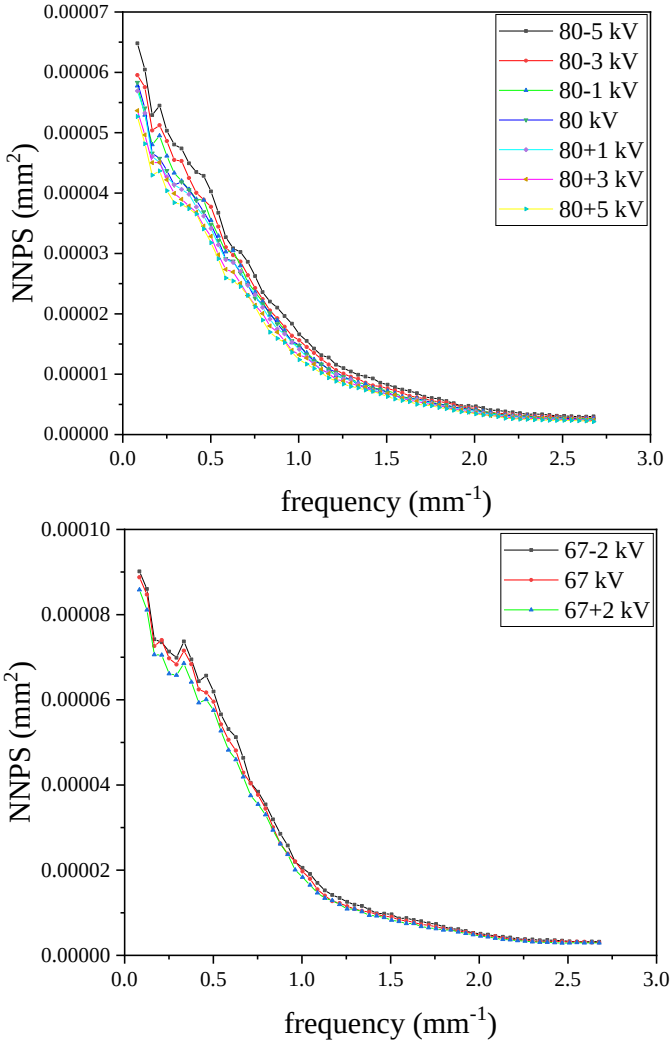

Figure 4-13. The NNPS measured at multiple tube voltage values. (Data: GE Definium)

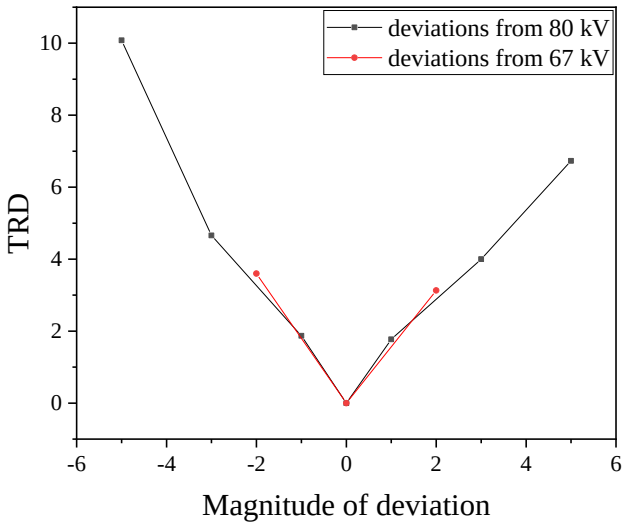

Figure 4-14. The TRD for different levels of deviation in tube voltage.

4.9 Defective Pixels

The uniform image acquired using the Siemens Luminos with the fixed pattern artifact is shown in figure (4-15). Figure (4-16) demonstrates some of the synthetic defective images composed from the real dataset images acquired using the GE Definium.

As illustrated in figure (4-17), in case of the GE Definium system, the NNPS was measured for uniform images with different levels of defective pixel artifacts. The results were then compared to the NNPS of an image with no defective pixels. According to figure (4-17), as the value of MSE, as an indicator of the level of defective pixel artifact existing in the image, increases, the resultant NNPS of the image increases as well.

Table (4-5) describes the properties of the images with defective pixel artifact and represents the TRD between the NNPS of these defective images and a reference image with no artifact. As shown in table (4-5), the TRD between the NNPS of an artifact-free image and an image with an MSE of 0.98 and only 192 defective pixels distributed over the image plane is 2.2. Figure (4-18) shows the NNPS for two uniform images with and without the artifact acquired on the Siemens system. The resultant NNPS is considerably increased for the image with the artifact. The TRD between the two plots is 4.6.

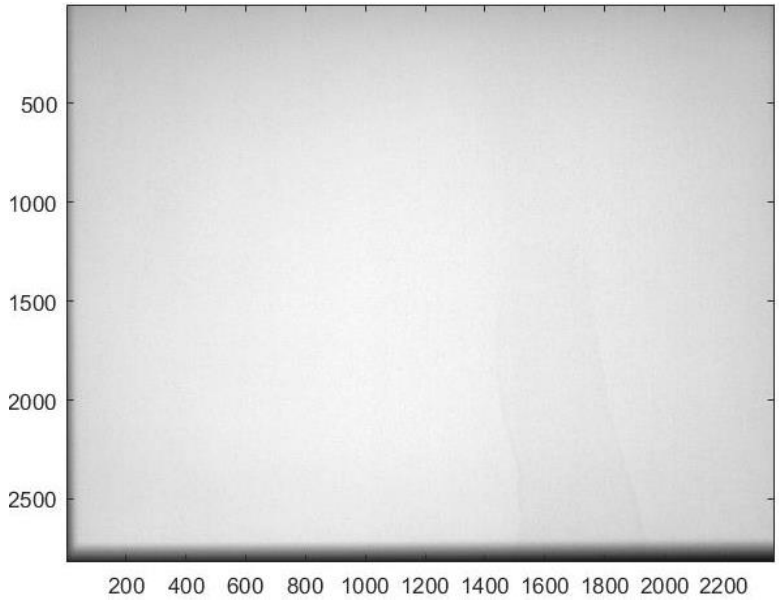

Figure 4-15. Uniform image acquired with Siemens Luminos unit with visible cluster of defective pixels on the right side.

Chapter 4: Results

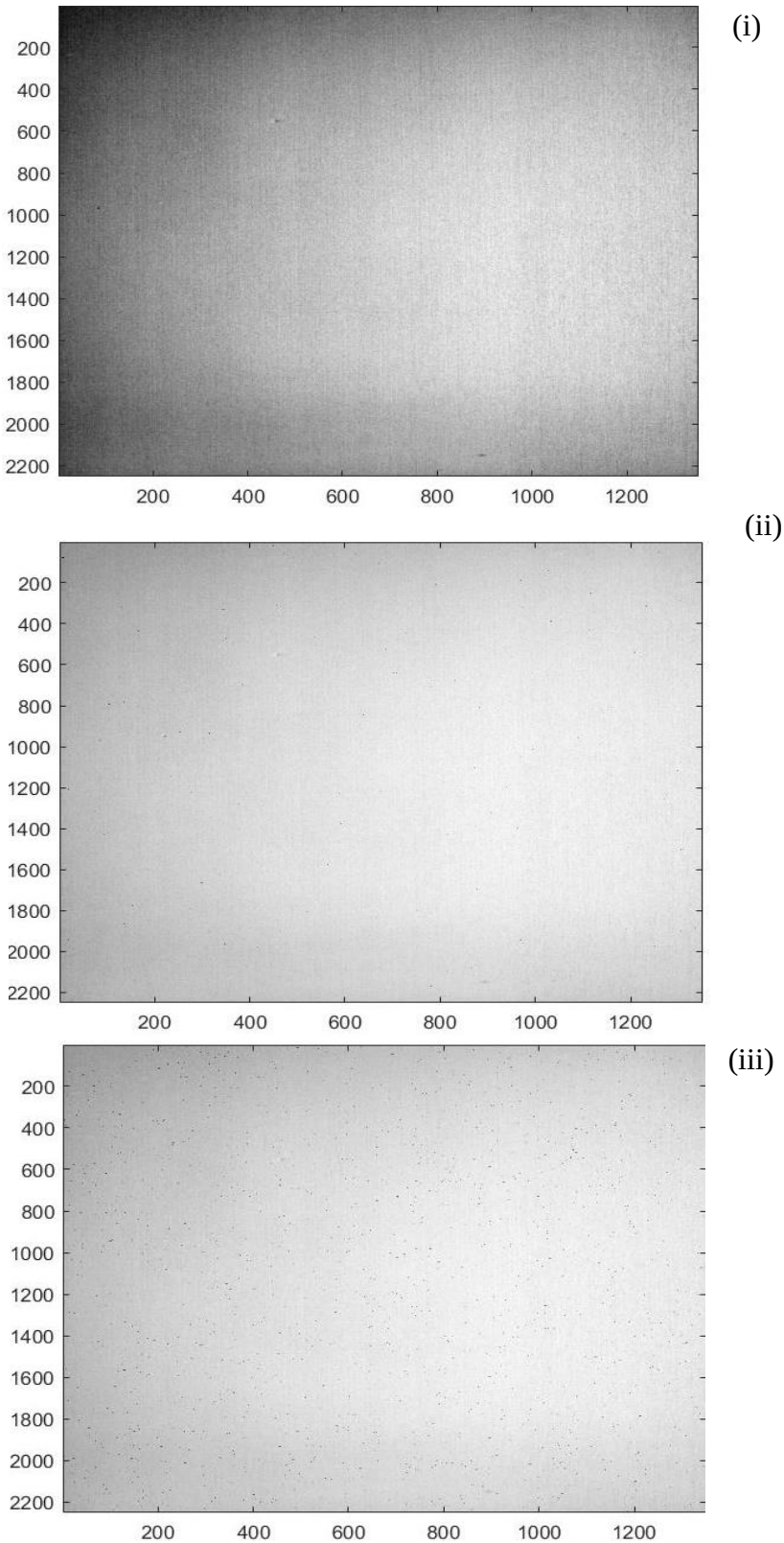

Figure 4-16. Uniform images with different levels of defective pixels. i) original image, ii) MSE 4.3 and iii) MSE 73.0.

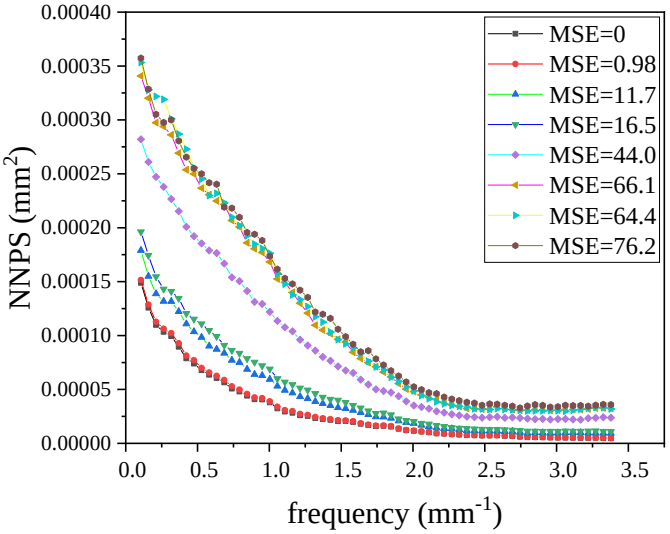

Figure 4-17. The NNPS of images with various amounts of defective pixels for GE Definium.

Table 4-5. The *TRD* between the NNPS of an image with no artifact and images with various amounts of defective pixels.

MSE	% of defective pixels	*TRD*
0.98	0.01	2.23
11.7	0.13	37.73
16.5	0.17	51.7
44.0	0.48	149.51
66.1	0.74	221.20
64.4	0.74	223.77
76.2	0.86	247.94

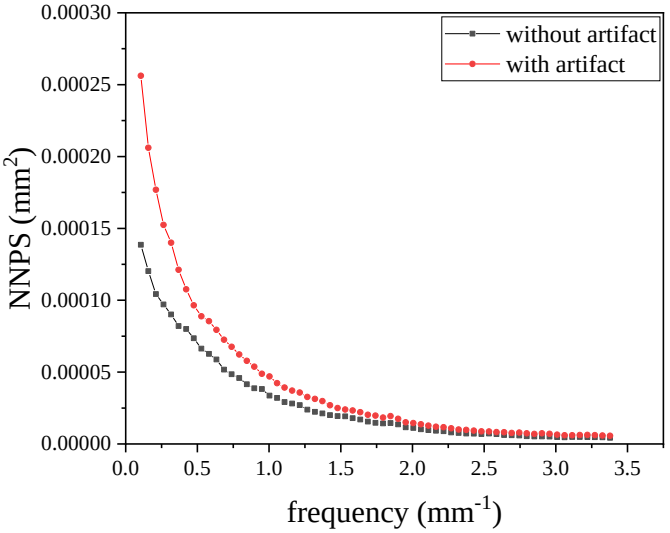

Figure 4-18. The NNPS measured for uniform images with and without fixed pattern artifact for Siemens Luminos.

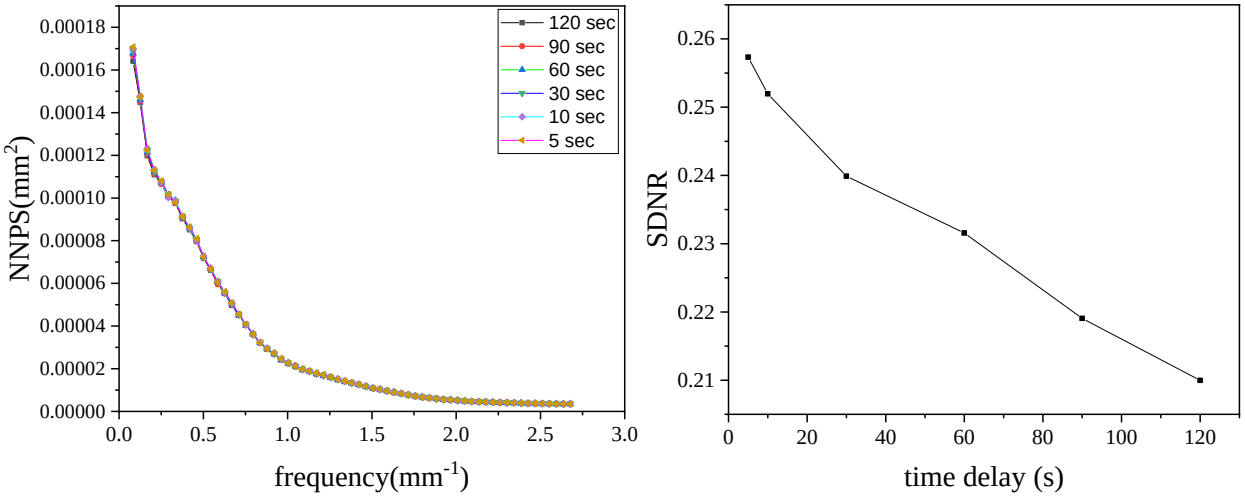

(i) (ii)

Figure 4-19. (i) The NNPS measured for uniform images with different levels of image lag, (ii) the SDNR measured for ROIs selected from the uniform images acquired after acquisition of an Al sheet with various time delays in betweene.

4.10 Image Lag

Figure (4-19) shows the NNPS and the SDNR calculated for six uniform images acquired after exposure of an aluminum sheet. The comparison of the calculated SDNR indicates that as the time interval between acquisition of two consecutive image decreases, the SDNR increases. The maximum TRD is 0.7. This TRD is obtained from the NNPS of the images acquired with delays of 5 and 120 seconds.

4.11 Mismatched Grid

As shown in Figure (4-20), when the grid focal distance is mismatched, observable periodic lines appear on the image. Figure (4-21) shows the NNPS calculated for two uniform images with the mismatched grid in and out. When the mismatched grid is used, the NNPS is higher, particularly at low frequencies and a notable local spike is observed at frequency range of [1.75-2] mm^{-1}. The TRD between the NNPS of images with and without the mismatched grid is 38.5 and 41.3 for 3.2 mAs and 5 mAs exposures, respectively.

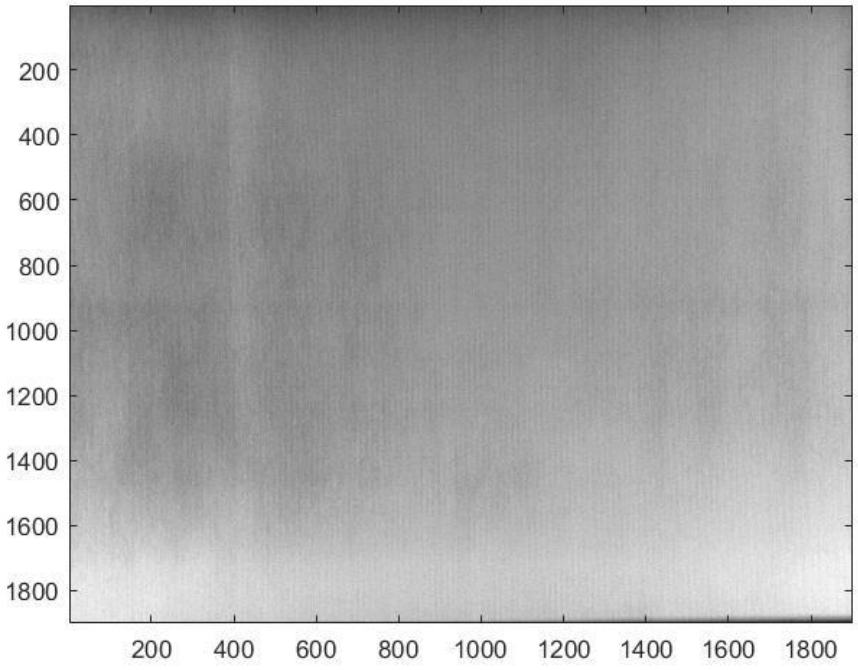

Figure 4-20. Uniform image with the mismatched grid in.

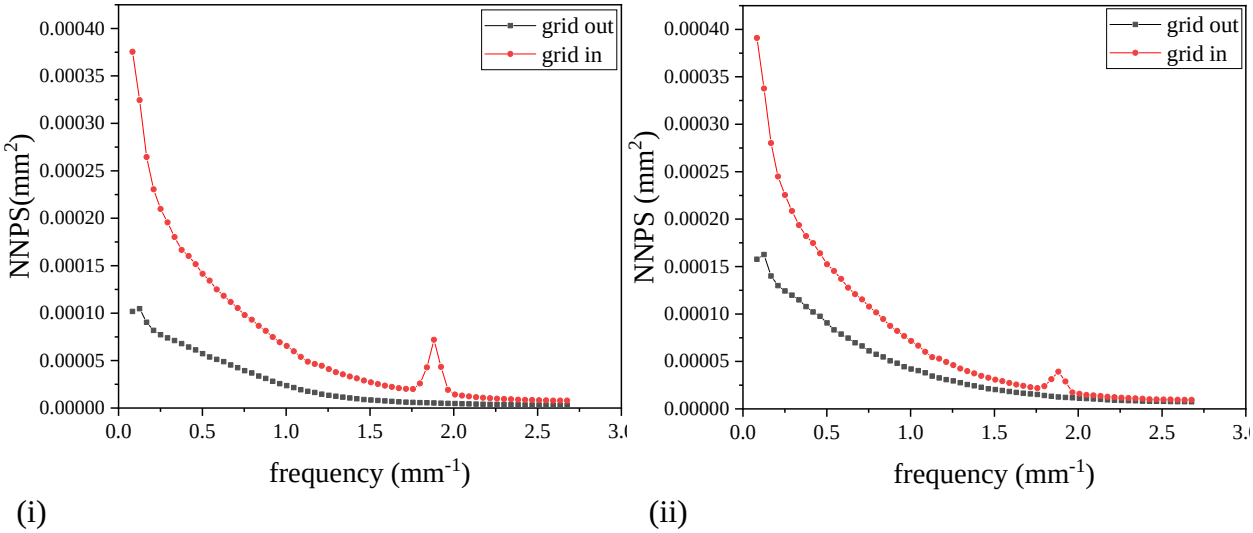

Figure 4-21. The NNPS measured for uniform images with the mismatched grid in and out for (i) 5 mAs and (ii) 3.2 mAs. (Data: GE Definium)

4.12 NPS Decomposition

The three components of the NPS decomposed using equation (2-22) are shown in figure (4-22). The fixed pattern and quantum coefficients derived from equation (2-22) and equation (3-6) are shown in figure (4-23). The absolute difference between each of these coefficients calculated for each frequency bin were computed, shown in figure (4-24). The difference is in the order of 10^{-7} for most of frequency bins for both coefficients. The maximum absolute difference is 7.03×10^{-5} and 2.01×10^{-4} between fixed pattern coefficients and quantum coefficients, respectively. The TRD was also calculated for the resultant coefficients. For fixed pattern coefficients calculated with and without electronic component, the TRD was equal to 8×10^{-7}. For quantum coefficients the TRD between them was equal to 2×10^{-6}. This suggests the electronic noise can be removed from the decomposition.

Figure (4-25) shows the two NPS decomposed coefficients for two selected values of tube voltage. The quantum and fixed pattern noise component of two images with 3 kV difference in tube voltage value were compared. The TRD between the fixed pattern and quantum coefficients are 12.14 and 8.27, respectively.

Figure (4-26) shows fixed pattern and quantum NPS coefficients for images acquired with large and small focal spot options on the system. The TRD was 62.43 and 30.73 for fixed pattern and quantum coefficients, respectively.

In figure (4-27), the fixed pattern and quantum NPS components of images with the 0.01% defective pixels are compared to their counterpart of images without the artifact. Both NPS components increased at almost all the frequency range after implementing the defective pixels in the image. However, the TRD calculated for fixed pattern component is considerably higher than the one calculated for quantum noise. The TRD for fixed pattern components and quantum components are 40.9 and 3.9.

The two noise components of the images acquired with and without the mismatched grid are illustrated in figure (4-28). The quantum noise was considerably higher when the grid was out. The fixed pattern noise shape was notably different when using the mismatched grid. The local spike observed on the total NNPS shown in figure (4-21), also appears in the fixed pattern component of the NPS but wasn't pronounce in quantum component when using the mismatched grid during the image acquisition. Table (4-6) lists the TRD between the noise components for each of the described performance deviations.

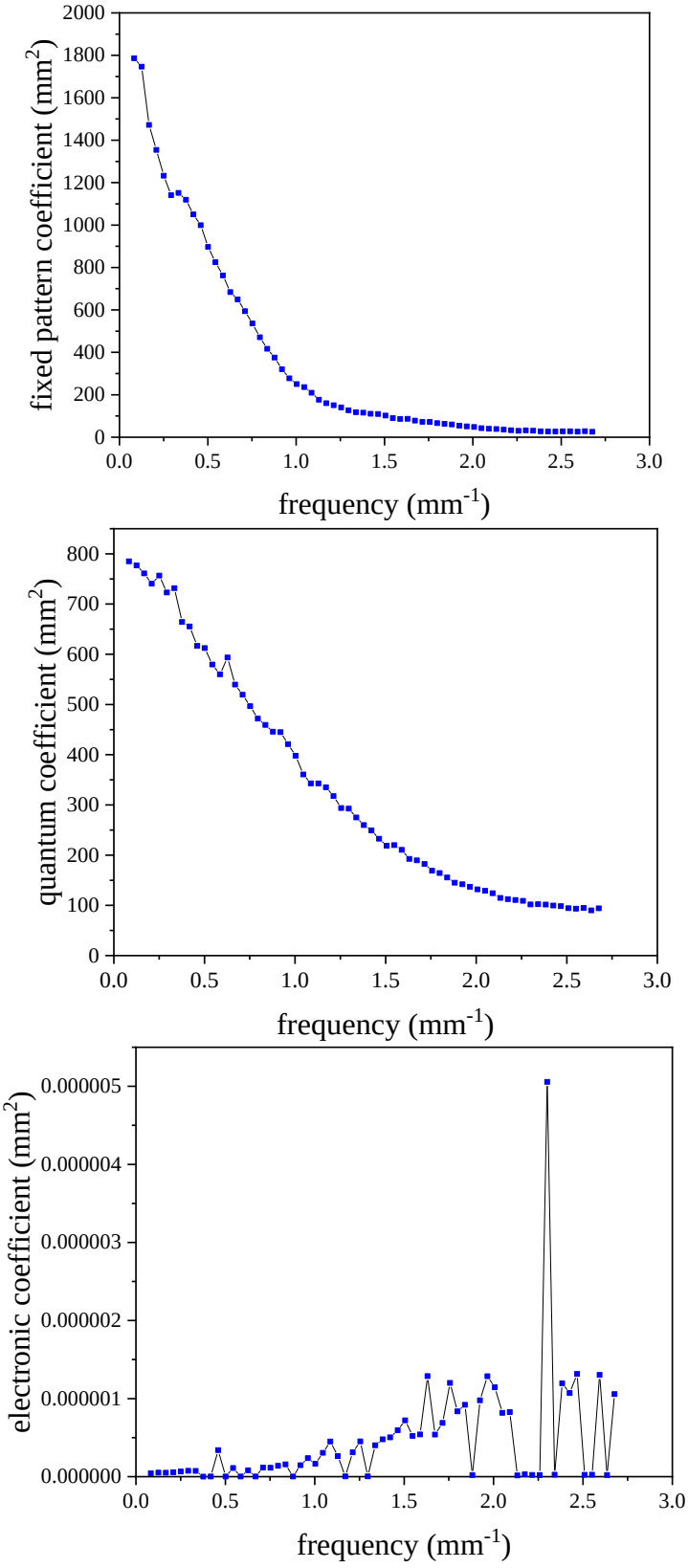

Figure 4-22. Three NPS components obtained by polynomial decomposition using equation (2-22) at 80 kV.

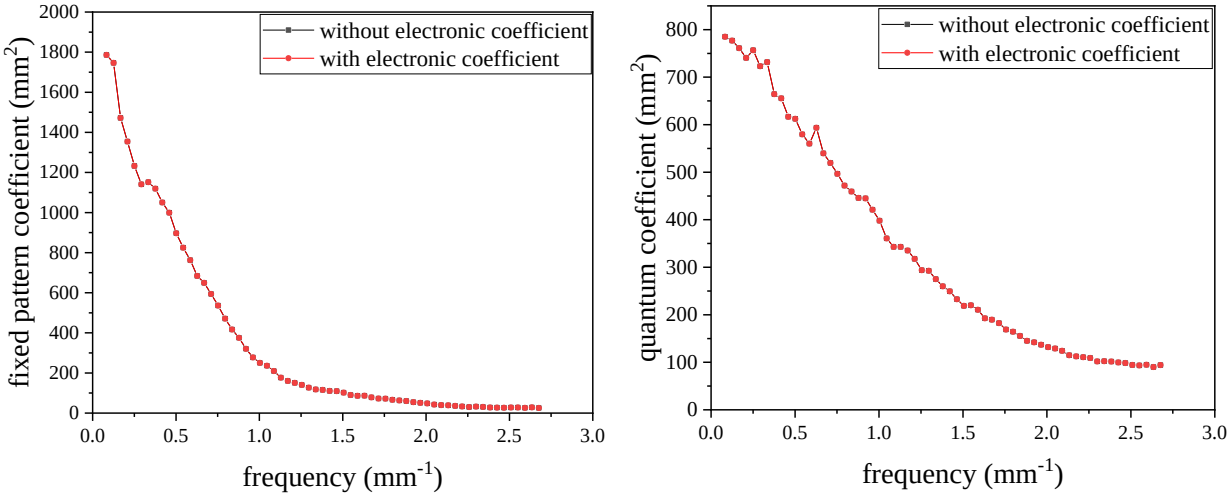

Figure 4-23. The fixed pattern and quantum coefficients derived from equations (3-6) and (2-22).

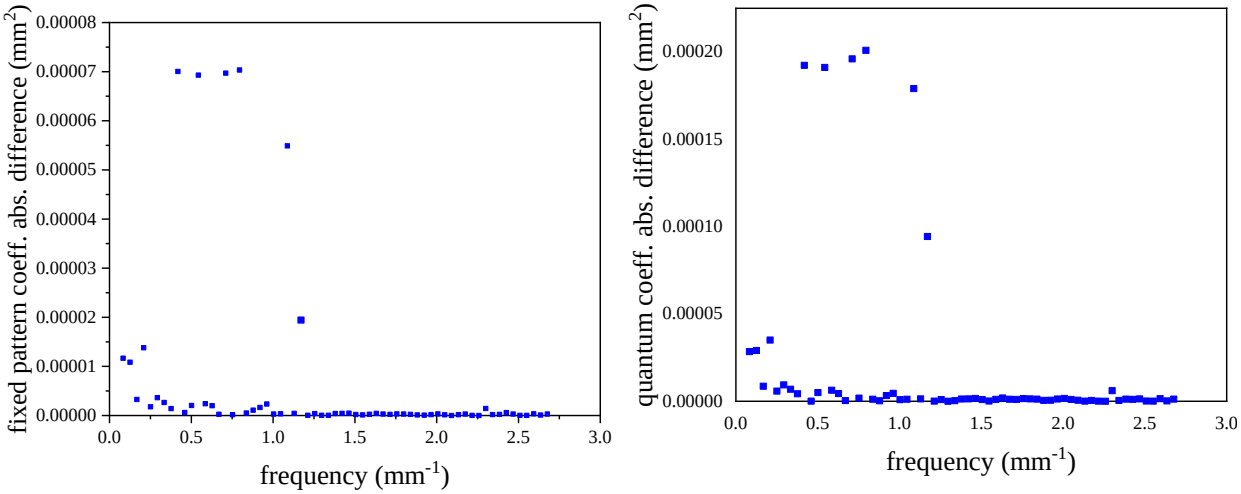

Figure 4-24. The magnitude of absolute difference between the fixed pattern coefficients and quantum coefficients derived from equations (2-22) and (3-6) for each frequency bin.

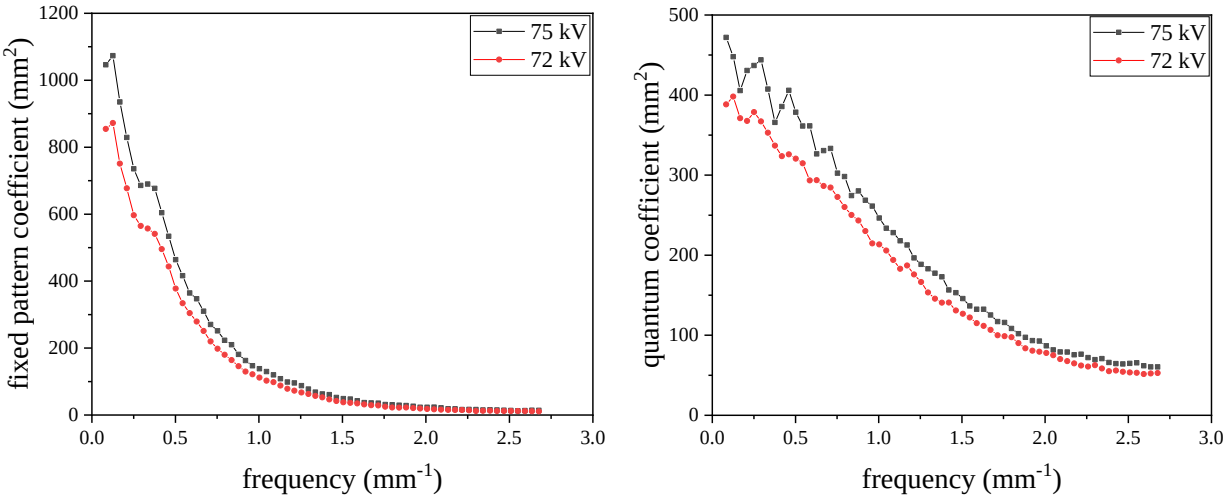

Figure 4-25. The fixed pattern and quantum NPS coefficients obtained by polynomial decomposition for 75 and 72 kV.

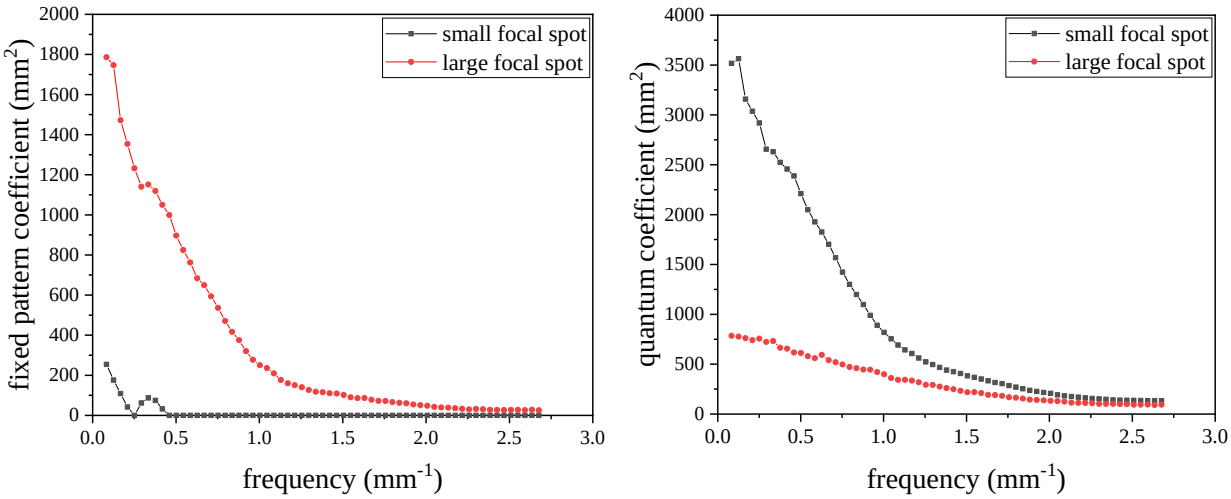

Figure 4-26. The fixed pattern and quantum NPS coefficients obtained by polynomial decomposition for small and large focal spot.

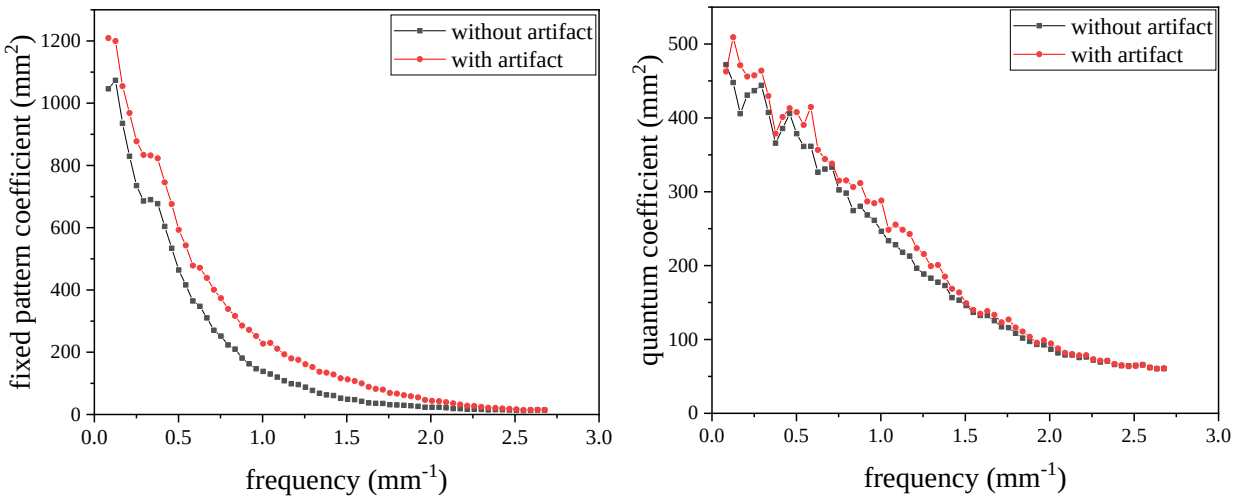

Figure 4-27. The fixed pattern and quantum NPS coefficients obtained by polynomial decomposition for images with and without defective pixels.

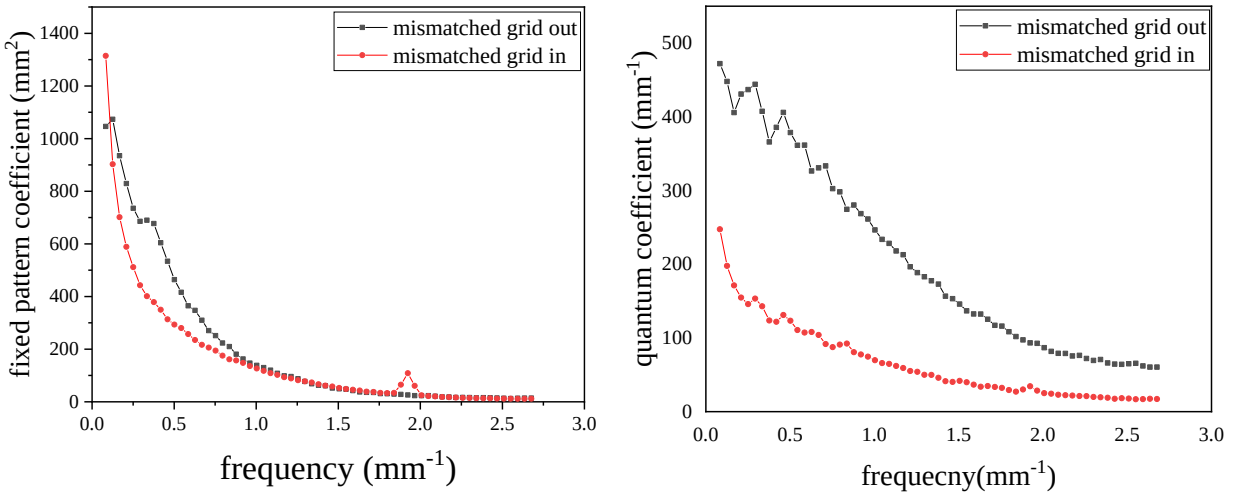

Figure 4-28. The fixed pattern and quantum NPS coefficients obtained by polynomial decomposition for images with and without mismatched grid.

Table 4-6. The TRD of the NPS components for different types of performance deviation.

Performance deviation type	TRD	
	Fixed pattern component	Quantum component
kV deviation	12.14	8.27
Focal spot size (resolution loss)	62.43	30.73
Defective pixels	40.92	3.9
Mismatched grid	15.44	44.02

Chapter 5

Discussion

Results confirm the linearity of both digital imaging systems' response functions over the exposure range of interest. In case of WSS and ergodicity assessment, according to figure (4-3) and (4-4), the noise is not constant over the image and the periphery of the image shows higher levels, particularly in case of the Siemens Luminos system. Results also show that the spatial average does not precisely represent the ensemble average. However, the variations in the noise pattern across the image plane, as well as the difference between the ensemble average and the spatial average, are small. Therefore, since the limitations resulted in the variations cannot be overcome and the variations are reasonably small, these assumptions can still be considered valid and acceptable.

The feasibility of the polynomial fit model used to detrend the noise image was verified by comparing it to a detrending using an average of 45 images. The comparison of the NNPS calculated for repeated image proves that the results are reproducible. The maximum TRD was 1.75, for the Siemens Luminos, and 0.7, for the GE Definium. Given that all measurements were performed at the same exposure level, these values represent the uncertainty of the NPS measurements due to exposure variations in this study. Therefore, these values were considered as the "threshold" of the NPS sensitivity to performance deviations.

The NNPS was calculated for various types of performance deviation and compared to a reference NNPS. For focal spot blooming, the TRD between the NNPS of two images was lower than the derived threshold of the NNPS sensitivity. Therefore, it can be concluded that since the change in focal spot size is well below the threshold, it does not have a considerable impact on the NPS. In case of resolution, as table (4-4) suggests, the value of TRD is bigger than the threshold

of the NPS sensitivity for both systems. Therefore, the results show that the NPS is sensitive to resolution changes.

Results show that an increase in tube voltage results in a decrease in the NNPS. A 1 kV deviation from 80 kV resulted in a TRD bigger than the NNPS threshold. As discussed earlier, safety reports recommend troubleshooting when tube voltage deviates from the selected value by 10%. However, the result indicates that the noise power spectrum is sensitive to much smaller changes in tube voltage value and deviations from the selected tube voltage as low as 1% of the nominal value impact the NNPS magnitude.

The comparison between the NNPS of images with and without defective pixels, for both systems used in this study, indicate that NPS is sensitive to defective pixel artifact and flat field artifact, as shown in figures (4-17) and (4-18). According to table (4-5), the TRD between the NNPS of an image with an MSE of 0.98 and 192 defective pixels over the image plane, and the original image was higher than the NNPS sensitivity threshold. In case of the Siemen Luminos, the TRD between the NNPS of images with and without the fixes pattern artifact was also greater than the NNPS threshold sensitivity for this system. According to figure (4-19), the comparison of the NNPS of uniform images collected after image acquisition of a high contrast object (aluminum sheet) indicates that the NNPS is not sensitive to the levels of image lag observed in this study. Though, it is possible that the NPS will detect excessive image lag.

The NNPS was also higher when using the mismatched grid which is due to the increase in fixed pattern noise. The frequency at which the pronounce spike was observed on the NNPS can correspond to the grid frequency. This well-localized spike shows that the NNPS is remarkably sensitive to fixed pattern changes in system performance.

Decomposition of the NPS was performed to study effects of various types of performance deviation on the noise components. In theory, the fixed pattern noise corresponds to deterministic component of the noise and is proportional to the square of photon fluence [28]. Quantum noise is related to stochastic component of the noise and is proportional to the square of modulation transfer function (MTF^2), aliasing, fill factor, etc. [25]. Electronic noise, however, is not related to MTF or photon fluence and is expected to appear as white noise. In this project, there were limitations on studying electronic noise since the DR system used for image acquisition would automatically apply dark current corrections on the output. Therefore, in this study, it was assumed that the

electronic noise coefficient in equation (2-23) is negligible and can be removed out of the equation. In order to verify this assumption, the NPS was decomposed into its three components for one case. The results confirm the electronic noise is negligible for the system used in this study and can be taken out of the decomposition equation. Therefore, the NPS coefficients were derived from equation (3-6).

Figure (4-25) shows that both fixed pattern and quantum coefficients increased at the higher tube voltage value. The difference is more pronounce for the fixed pattern noise which is in line with the fact that fixed pattern noise is proportional to the square of photon fluence. Quantum noise is also associated with the absorption of primary and secondary x ray photons. Any change in tube voltage affects the average photon energy and results in variation in penetration power of x ray photons and fluctuations in the number of absorbed secondary photons by the detector. This explanation is in line with the observed change in the quantum coefficient.

Figure (4-26) shows the two NPS components for two images acquired with large and small focal spots. A significant decrease was observed in the quantum component of the NPS when using the large focal spot for image acquisition. This result agrees with the fact that quantum noise is proportional to the square of the MTF. Selecting large focal spot results in a lower MTF. There was also a notable increase in the fixed pattern noise component. The structural change (focal spot size) applied during the image acquisition resulted in observing this considerable increase in the fixed pattern (structure) noise component.

According to table (4-13), the TRD calculated for fixed pattern component (40.9) is considerably bigger than the one calculated for quantum noise (3.1). This result is consistent with the fact that defective pixels is a structured artifact in the system and Therefore, it is expected to mostly affect the fixed pattern noise.

The resultant fixed pattern and quantum noise components of the images acquired with and without the mismatched grid shows that the quantum noise is considerably smaller when the mismatched grid is used. The reason behind this is that when the image is acquired with the grid, a great portion of x ray photons are absorbed and less photons reach the detector. A local spike was observed on the fixed pattern NPS coefficient when the grid was used. This result proves that the local spike observed on the total NPS (shown in figure 4-21) was due to the presence of a fixed pattern artifact in the imaging system.

The noise decomposition results suggest that the affected noise coefficient is associated with the type of performance deviation. Deviation in exposure quality affected both fixed pattern and quantum components. When resolution loss was added to the system's output, the most pronounce change was observed in quantum noise. The fixed pattern component was also the most influenced when a structural change occurred such as the addition of dead pixel artifact, using a mismatched grid and changing the size of focal spot.

Chapter 6

Conclusion and Future Work

This thesis investigated the NPS as a general constancy test in quality control routines for digital radiology which is sensitive to deviations in various performance parameters.

Two digital x ray units were used in this study: GE Definium and Siemens Luminos. The linearity of detector response function was confirmed for both systems. The noise was found to be non-uniform and non-stationary over the image plane for both systems. Since these variations were small and negligible, this study assumed that the stationarity and ergodicity assumptions are valid for the system noise behaviour.

The accuracy of the polynomial fit model used to compute the NPS was confirmed by comparing it to the average of 45 uniform images. The reproducibility of the NPS calculation was assessed by comparing repeated images with the same loading factors.

In order to evaluate the sensitivity of the NPS as general constancy test to various deviations in the system's performance, the effect of six types of deviation on the NNPS was investigated: focal spot blooming, resolution change, tube voltage change, defective pixels, image lag and mismatched grid. The NPS was insensitive to focal spot blooming and image ghosting, and sensitive to resolution, tube voltage change, defective pixel and fixed pattern artifacts.

The effect of tube voltage change, focal spot size, defective pixels and grid performance on quantum and fixed pattern components of the NPS shows that the resultant change in these components corresponds to the type of change introduced to the system. The fixed pattern changes impacted the fixed pattern NPS component the most. The changes associated with quantum noise affected the quantum component.

In conclusion, this thesis proposes the NPS as a general constancy test which is sensitive to many possible sources of degradation in digital imaging system performance. Since the imaging system used to collect the dataset automatically corrected the images for dark noise, there was limitations on studying the impact of the electronic defects on the NPS and its components. Possible future work can include investigation of the sensitivity of the NPS to electronic degradations. machine learning could be used to identify possible sources of system performance degradation. A practical extension of this work is to pilot it as part of the QC of clinical systems and implement the NPS calculation algorithm on the imaging systems themselves.

Appendix A

NPS Coefficients

The NPS coefficients were derived according to equation (3-6) for each frequency bin separately. Tables (A-1) to (A-4) represent the magnitude of the NPS coefficients for each of the frequency bins calculated for the types of performance deviations studied in this thesis.

Table A-1. Fixed pattern and quantum NPS coefficients cfor each frequency bin at 75 and 72 kV.

Frequency (mm^{-1})	Fixed pattern coefficient (mm^2) (75 kV)	Fixed pattern coefficient (mm^2) (72 kV)	Quantum coefficient (mm^2) (75 kV)	Quantum coefficient (mm^2) (72 kV)
0.084	1046.061	854.605	471.963	388.294
0.125	1073.229	872.200	447.896	398.072
0.167	935.054	750.888	405.672	371.026
0.209	829.246	677.435	430.689	367.695
0.251	735.285	596.858	436.840	378.699
0.293	685.873	564.842	443.953	367.041
0.335	689.868	556.868	407.395	352.966
0.376	676.977	540.930	365.857	336.772
0.418	604.181	495.698	385.659	323.660
0.460	533.899	443.490	405.890	325.939
0.502	463.948	377.662	378.536	320.501
0.544	416.030	333.991	361.297	314.801
0.586	364.499	304.409	361.441	293.401
0.627	347.243	279.328	326.429	293.608
0.669	310.067	250.848	330.664	286.418
0.711	270.507	219.606	333.234	284.519
0.753	251.508	198.071	302.413	272.694
0.795	223.193	180.137	298.120	260.120
0.836	209.803	163.936	274.383	250.171
0.878	181.030	145.827	280.204	243.299
0.920	162.806	129.895	268.605	230.143
0.962	146.994	121.432	261.211	214.727
1.004	138.214	111.634	246.439	213.467
1.046	129.896	102.627	233.631	205.837

Table (A-1) (continued).

1.0874	120.059	98.004	228.168	194.053
1.129	108.232	87.988	218.011	182.939
1.171	98.474	78.513	212.741	187.024
1.213	95.923	72.840	196.505	175.948
1.255	87.659	67.361	188.543	166.489
1.297	77.383	62.782	182.944	153.467
1.338	68.144	56.975	177.523	145.656
1.380	62.770	52.667	172.944	140.607
1.422	60.876	46.502	156.537	140.767
1.464	52.398	41.916	153.120	130.934
1.506	49.038	38.146	145.800	126.779
1.547	47.409	36.366	136.606	122.073
1.589	42.293	34.541	132.509	115.073
1.631	37.169	31.729	132.398	111.706
1.673	35.868	29.269	125.300	106.737
1.715	35.314	28.626	117.036	99.928
1.756	31.186	24.932	115.956	98.742
1.798	30.671	22.578	108.419	97.445
1.840	29.321	22.0923	101.841	90.116
1.882	28.106	22.323	97.353	83.622
1.924	26.088	20.675	93.264	80.729
1.966	23.230	19.515	92.691	79.327
2.007	23.172	18.155	86.743	77.804
2.049	23.323	16.933	81.700	75.043
2.091	21.239	15.957	79.087	70.258
2.133	18.808	15.184	78.933	67.638
2.175	18.461	14.779	75.526	64.860
2.217	16.438	14.849	76.256	62.153
2.258	16.622	13.996	72.093	60.812
2.300	16.244	11.764	69.508	62.511
2.342	14.800	12.661	70.705	58.474
2.384	15.586	12.775	65.939	55.059
2.426	15.106	11.808	64.489	55.835
2.466	14.386	11.850	64.096	54.349
2.509	13.612	12.029	64.885	53.485
2.551	12.399	11.725	65.535	53.075
2.593	13.393	11.682	61.896	51.524
2.635	14.218	11.108	60.465	52.239
2.677	14.087	10.931	60.474	52.754

Table 7-2. Fixed pattern and quantum NPS coefficients for each frequency bin at small and large focal spot size.

Frequency (mm^{-1})	Fixed pattern coefficient (mm^2) (small F.S)	Fixed pattern coefficient (mm^2) (Large F.S)	Quantum coefficient (mm^2) (small F.S)	Quantum coefficient (mm^2) (Large F.S)
0.084	254.312	1785.870	3516.289	785.108
0.125	176.240	1746.477	3563.242	776.981
0.167	108.838	1471.748	3157.853	760.964
0.209	41.883	1354.013	3036.245	740.481
0.251	4.0E-08	1232.259	2918.356	756.577
0.293	61.619	1140.955	2656.194	723.028
0.335	86.924	1151.553	2629.930	731.721
0.376	74.457	1119.066	2523.767	664.285
0.418	32.216	1050.283	2456.347	655.464
0.460	1.4E-07	999.111	2388.065	616.611
0.502	1.5E-06	896.747	2210.064	612.345
0.544	5.7E-08	824.777	2048.366	579.496
0.586	5.9E-08	762.282	1927.489	560.191
0.627	1.3E-05	684.017	1824.543	593.437
0.669	6.5E-08	649.345	1703.059	539.736
0.711	4.6E-08	593.876	1568.188	519.344
0.753	1.6E-08	536.209	1423.229	496.507
0.795	2.3E-08	471.066	1300.347	471.710
0.836	3.2E-08	416.416	1197.386	459.282
0.878	2.2E-08	375.413	1097.906	445.762
0.920	1.7E-08	320.386	989.533	444.882
0.962	1.7E-08	277.518	889.900	421.143
1.004	1.4E-08	250.031	819.087	398.011
1.046	1.1E-10	236.167	753.719	360.640
1.087	6.9E-07	209.186	691.225	342.815
1.129	1.4E-08	176.766	643.195	342.881
1.171	2.0E-08	160.428	606.942	335.027
1.213	1.4E-08	150.327	562.123	317.654
1.255	1.4E-08	140.471	523.492	293.673
1.297	1.3E-08	126.741	496.350	292.537
1.338	1.4E-08	117.618	467.063	274.944
1.380	1.5E-10	115.406	440.505	259.855
1.422	2.3E-08	110.472	424.966	249.342
1.464	1.9E-08	109.163	406.762	232.700
1.506	1.8E-08	102.026	383.014	218.776
1.547	2.6E-08	89.833	368.264	219.867
1.589	2.0E-08	86.3107	350.610	210.482
1.631	2.0E-10	86.374	332.320	192.544
1.673	2.3E-08	78.064	316.260	189.653

Table (A-2) (continued).

1.715	2.5E-10	72.343	304.345	182.368
1.757	5.4E-06	72.080	285.425	168.913
1.798	2.4E-08	66.219	269.770	164.373
1.840	2.3E-08	62.748	253.657	155.515
1.882	2.9E-08	60.227	237.201	145.092
1.924	3.4E-08	54.530	226.263	141.891
1.966	6.4E-06	51.163	216.202	136.814
2.007	2.7E-08	47.876	206.761	131.926
2.049	3.3E-08	42.705	192.265	128.912
2.091	7.5E-06	39.369	182.612	124.069
2.133	3.7E-08	38.442	175.052	114.811
2.175	7.6E-06	35.946	168.534	112.426
2.217	3.3E-08	33.072	161.398	110.629
2.258	3.5E-06	30.180	156.503	109.087
2.300	3.4E-06	32.048	151.525	101.878
2.342	3.2E-08	30.505	146.740	102.133
2.384	3.3E-06	27.979	141.582	101.604
2.426	3.4E-08	27.390	139.702	99.689
2.468	3.7E-06	26.679	138.680	98.412
2.509	3.6E-06	27.729	136.653	94.283
2.551	3.7E-08	27.671	135.942	93.456
2.593	3.8E-06	26.190	133.679	94.745
2.635	3.8E-08	28.033	133.721	90.050
2.677	3.9E-08	25.633	133.934	94.047

Table 7-3. Fixed pattern and quantum NPS coefficients for each frequency bin for images with and without defective pixels artifact.

Frequency (mm^{-1})	Fixed pattern coefficient (mm^{-2}) with artifact	Fixed pattern coefficient (mm^{-2}) without artifact	Quantum coefficient (mm^{-2}) with artifact	Quantum coefficient (mm^{-2}) without artifact
0.084	1208.934	1046.061	462.872	471.963
0.125	1199.551	1073.229	509.195	447.896
0.167	1054.724	935.054	471.154	405.672
0.209	968.497	829.246	456.012	430.689
0.251	877.694	7.4E+02	457.544	436.840
0.293	833.897	685.873	463.900	443.953
0.335	832.077	689.868	429.715	407.395
0.376	822.726	676.977	378.688	365.857
0.418	745.507	604.181	401.133	385.659
0.460	676.023	5.3E+02	412.965	405.890
0.502	593.275	4.6E+02	407.660	378.536

Table (A-3) (continued).

0.544	543.091	4.2E+02	390.374	361.297
0.586	478.398	3.6E+02	414.794	361.441
0.627	471.149	3.5E+02	356.599	326.429
0.669	438.774	3.1E+02	344.136	330.664
0.711	400.817	2.7E+02	338.147	333.234
0.753	373.355	2.5E+02	315.153	302.413
0.795	338.923	2.2E+02	315.316	298.120
0.836	316.291	2.1E+02	306.350	274.383
0.878	285.467	1.8E+02	311.694	280.204
0.920	272.094	1.6E+02	286.909	268.605
0.962	251.912	1.5E+02	284.486	261.211
1.004	227.289	1.4E+02	287.922	246.439
1.046	229.998	1.3E+02	248.425	233.631
1.087	211.348	1.2E+02	255.405	228.168
1.129	193.022	1.1E+02	248.523	218.011
1.171	180.113	9.9E+01	242.755	212.741
1.213	175.556	9.6E+01	223.568	196.505
1.255	161.104	8.9E+01	215.591	188.543
1.297	152.314	7.7E+01	199.225	182.944
1.338	137.301	6.8E+01	200.772	177.523
1.380	134.484	6.3E+01	185.127	172.944
1.422	128.351	6.1E+01	168.527	156.537
1.464	116.405	5.2E+01	163.637	153.120
1.506	112.545	4.9E+01	148.955	145.800
1.547	107.304	4.7E+01	139.931	136.606
1.589	99.676	4.2E+01	134.746	132.509
1.631	88.511	3.7E+01	138.334	132.398
1.673	82.446	3.6E+01	133.249	125.300
1.715	79.782	3.5E+01	123.087	117.036
1.757	69.177	3.1E+01	127.050	115.956
1.798	66.890	3.1E+01	116.209	108.419
1.840	61.959	2.9E+01	110.719	101.841
1.882	58.479	2.8E+01	103.544	97.353
1.924	54.740	2.6E+01	95.529	93.264
1.966	46.862	2.3E+01	98.7845	92.691
2.007	43.858	2.3E+01	94.463	86.743
2.049	42.813	2.3E+01	87.853	81.700
2.091	39.286	2.1E+01	81.842	79.087
2.133	35.597	1.9E+01	80.119	78.933
2.175	32.168	1.9E+01	78.408	75.526
2.217	28.052	1.6E+01	78.618	76.256

Table (A-3) (continued).

2.258	27.128	1.7E+01	73.204	72.093
2.300	24.290	1.6E+01	71.301	69.508
2.342	21.868	1.5E+01	71.208	70.705
2.384	20.987	1.6E+01	66.857	65.939
2.426	19.243	1.5E+01	65.059	64.488
2.468	17.915	1.4E+01	63.658	64.096
2.509	16.563	1.4E+01	64.031	64.885
2.551	14.166	1.2E+01	65.667	65.535
2.593	14.630	1.3E+01	61.953	61.896
2.635	14.975	1.4E+01	60.578	60.465
2.677	14.430	1.4E+01	60.965	60.474

Table 7-4. Fixed pattern and quantum NPS coefficients for each frequency bin for images: (a): with and (b): without the mismatched grid.

Frequency (mm^{-1})	Fixed pattern coefficient (mm^{-2}) (a)	Fixed pattern coefficient (mm^{-2}) (b)	Quantum coefficient (mm^{-2}) (a)	Quantum coefficient (mm^{-2}) (b)
0.084	1314.421	1046.061	247.341	471.963
0.125	902.450	1073.229	197.656	447.896
0.167	701.529	935.054	171.296	405.672
0.209	588.965	829.246	154.717	430.689
0.251	511.525	7.4E+02	145.886	436.840
0.293	442.905	685.873	153.357	443.953
0.335	401.082	689.868	142.938	407.395
0.376	378.618	676.977	123.553	365.857
0.418	349.923	604.181	121.908	385.659
0.460	313.175	5.3E+02	131.103	405.890
0.502	293.230	4.6E+02	123.272	378.536
0.544	280.116	4.2E+02	110.627	361.297
0.586	257.342	3.6E+02	107.314	361.441
0.627	234.882	3.5E+02	108.018	326.429
0.669	216.346	3.1E+02	103.954	330.664
0.711	206.111	2.7E+02	91.655	333.234
0.753	194.564	2.5E+02	87.464	302.413
0.795	175.529	2.2E+02	90.922	298.120
0.836	161.394	2.1E+02	92.255	274.383
0.878	157.058	1.8E+02	80.623	280.204

Table (A-4) (continued).

0.920	147.594	1.6E+02	77.515	268.605
0.962	135.833	1.5E+02	74.522	261.211
1.004	126.435	1.4E+02	69.754	246.439
1.046	117.523	1.3E+02	65.797	233.631
1.087	108.522	1.2E+02	64.817	228.168
1.129	102.482	1.1E+02	61.99	218.011
1.171	93.473	9.9E+01	59.195	212.741
1.213	88.677	9.6E+01	55.150	196.505
1.255	81.818	8.8E+01	54.068	188.543
1.297	77.827	7.7E+01	49.931	182.944
1.338	73.306	6.8E+01	49.781	177.523
1.380	66.869	6.3E+01	45.955	172.944
1.422	61.582	6.1E+01	41.271	156.537
1.464	58.087	5.2E+01	40.374	153.120
1.506	52.623	4.9E+01	41.686	145.800
1.547	48.738	4.7E+01	39.863	136.606
1.589	46.012	4.2E+01	36.567	132.509
1.631	42.915	3.7E+01	33.816	132.398
1.673	38.733	3.6E+01	34.722	125.300
1.715	37.213	3.5E+01	33.490	117.036
1.757	33.979	3.1E+01	32.216	115.956
1.798	33.224	3.1E+01	29.236	108.419
1.840	33.770	2.9E+01	27.078	101.841
1.882	64.748	2.8E+01	29.993	97.353
1.924	108.609	2.6E+01	34.388	93.264
1.966	60.810	2.3E+01	28.557	92.691
2.007	24.591	2.3E+01	25.091	86.743
2.049	21.615	2.3E+01	24.272	81.700
2.091	20.313	2.1E+01	22.808	79.087
2.133	18.104	1.9E+01	22.253	78.933
2.175	17.313	1.9E+01	21.802	75.526
2.217	16.120	1.6E+01	21.214	76.256
2.258	14.882	1.7E+01	20.974	72.093
2.300	14.572	1.6E+01	19.900	69.508
2.342	13.773	1.5E+01	19.513	70.705
2.383	13.288	1.6E+01	18.868	65.939
2.426	13.339	1.5E+01	17.411	64.488
2.468	12.251	1.4E+01	18.195	64.096

Table (A-4) (continued).

2.509	12.026	1.4E+01	17.681	64.885
2.551	11.951	1.2E+01	16.817	65.535
2.593	11.662	1.3E+01	16.891	61.896
2.635	11.392	1.4E+01	17.495	60.465
2.677	11.823	1.4E+01	17.133	60.474

The NNPS was calculated from the coefficients by inserting them into equation (3-6) for each frequency bin at an exposure level (0.5 mAs). In figure (A-1), two calculated NNPS are shown: 1) the one calculated using equation (3-2) is referred to as the "original method", 2) the one calculated by inserting coefficients into equation (3-6) is referred to as the "coefficient method". The magnitude of both NNPS and the relative difference between them for each frequency bin is shown in table (A-5).

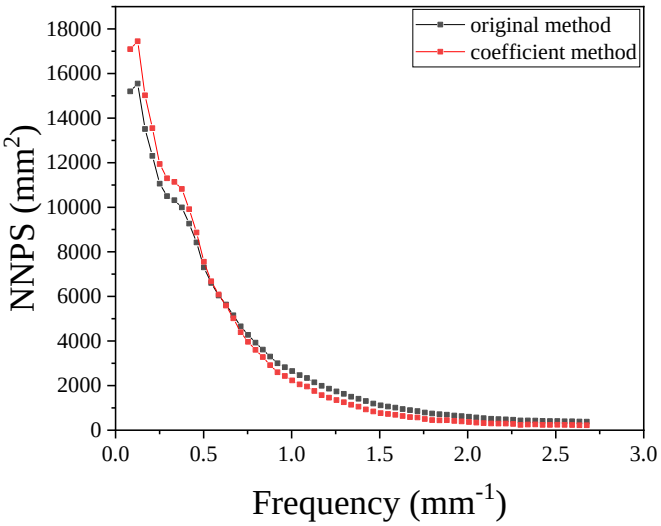

Figure 7-1. The NNPS calculated using coefficients and using equation (3-2) for the same image.

Table 7-5. The NNPS derived from coefficients and calculated using equation (3-2) and their relative difference for each frequency bin.

Frequency (mm^{-1})	NNPS (mm^2) by original method	NNPS (mm^2) by coefficients method	Relative difference $(\frac{abs(A-B)}{B})$
0.084	15199.99	17092.10	0.12
0.125	15548.18	17444.01	0.12
0.167	13508.72	15017.76	0.11
0.209	12304.69	13548.70	0.10
0.251	11058.71	11937.17	0.08
0.293	10499.32	11296.85	0.08
0.335	10312.12	11137.37	0.08
0.376	9993.10	10818.60	0.08
0.418	9268.53	9913.96	0.07
0.460	8419.95	8869.79	0.05
0.502	7305.13	7553.25	0.03
0.544	6606.18	6679.83	0.01
0.586	6041.02	6088.19	0.01
0.627	5634.92	5586.57	0.01
0.669	5153.87	5016.97	0.03
0.711	4659.83	4392.13	0.06
0.753	4273.01	3961.43	0.07
0.795	3924.26	3602.74	0.08
0.836	3614.71	3278.72	0.09
0.878	3301.88	2916.55	0.12
0.920	2998.89	2597.90	0.13
0.962	2821.11	2428.65	0.14
1.004	2651.77	2232.69	0.16
1.046	2469.27	2052.53	0.17
1.087	2339.53	1960.08	0.16
1.129	2146.80	1759.76	0.18
1.171	1989.55	1570.26	0.21
1.213	1858.07	1456.80	0.21
1.255	1738.38	1347.23	0.23
1.297	1627.49	1255.64	0.23
1.338	1499.61	1139.49	0.24
1.380	1411.40	1053.33	0.25
1.422	1308.55	930.03	0.29
1.464	1195.56	838.32	0.30
1.506	1113.01	762.92	0.31
1.547	1058.73	727.32	0.31
1.589	1008.39	690.81	0.31
1.631	948.25	634.57	0.33

Table (A-5) (continued).

1.673	896.44	585.38	0.34
1.715	854.51	572.52	0.33
1.757	788.26	498.64	0.37
1.798	746.35	451.56	0.39
1.840	713.28	441.85	0.38
1.882	691.71	446.45	0.35
1.924	655.61	413.50	0.37
1.966	628.81	390.30	0.37
2.007	602.03	363.10	0.39
2.049	570.90	338.6542	0.41
2.0911	535.96	319.1475	0.40
2.133	510.31	303.6784	0.40
2.175	492.73	295.5863	0.40
2.217	486.65	296.9835	0.39
2.258	467.57	279.9135	0.40
2.300	433.72	235.2817	0.46
2.342	436.95	253.2221	0.42
2.384	427.63	255.5097	0.40
2.426	411.99	236.1692	0.42
2.468	407.54	237.0066	0.42
2.509	407.08	240.5737	0.41
2.551	400.63	234.5082	0.41
2.593	395.27	233.6433	0.40
2.635	386.13	222.167	0.42
2.677	383.94	218.614	0.43

Bibliography

[1] Health Canada, *Radiation Protection in Radiology — Large Facilities Safety Procedures for the Installation , Use and Control of X-ray Equipment in Large Medical Radiological Facilities Safety Code 35*. 2008.

[2] P. Chaloner *et al.*, “Diagnostic X-Ray Imaging Quality Assurance: An Overview" ,” vol. 27, no. 4, pp. 171–177, 1996.

[3] E. Mah, E. Samei, and D. J. Peck, “Evaluation of a quality control phantom for digital chest radiography.,” *J. Appl. Clin. Med. Phys.*, vol. 2, no. 2, pp. 90–101, 2001, doi: 10.1120/jacmp.v2i2.2621.

[4] M. Korner, C. H. Weber, S. Wirth, K.-F. Pfeifer, M. F. Reiser, and M. Treitl, “Advances in Digital Radiography : Physical,” *Radiol. Soc. North Am.*, vol. 27, no. 3, pp. 675–686, 2007, doi: http://dx.doi.org/10.1148/rg.273065075.

[5] M. B. Williams *et al.*, “Digital Radiography Image Quality: Image Acquisition,” *J. Am. Coll. Radiol.*, vol. 4, no. 6, pp. 371–388, 2007, doi: 10.1016/j.jacr.2007.02.002.

[6] “ICRP Publication 103 The 2007 Recommendations of the International Commission on Radiological Protection,” *Ann ICRP*, vol. ICRP publi, pp. 37:1–332, 2007.

[7] C. Schaefer-Prokop, U. Neitzel, H. W. Venema, M. Uffmann, and M. Prokop, “Digital chest radiography: An update on modern technology, dose containment and control of image quality,” *Eur. Radiol.*, vol. 18, no. 9, pp. 1818–1830, 2008, doi: 10.1007/s00330-008-0948-3.

[8] A. K. Jones *et al.*, “Ongoing quality control in digital radiography: Report of AAPM Imaging Physics Committee Task Group 151,” *Med. Phys.*, vol. 42, no. 11, pp. 6658–6670, 2015, doi: 10.1118/1.4932623.

[9] B. JT, *The essential physics of medical imaging*. 2002.

[10] L. Lança and A. Silva, “Digital radiography detectors - A technical overview: Part 1,” *Radiography*, vol. 15, no. 1, pp. 58–62, 2009, doi: 10.1016/j.radi.2008.02.004.

[11] H. G. Chotas, J. T. Dobbins, and C. E. Ravin, “Principles of digital radiography with large-area, electronically readable detectors: A review of the basics,” *Radiology*, vol. 210, no. 3, pp. 595–599, 1999, doi: 10.1148/radiology.210.3.r99mr15595.

[12] E. Samei, “Performance of digital radiographic detectors: Quantification and Assessment Method,” *Adv. Digit. Radiogr.*, pp. 49–61, 2003.

[13] P. Sprawls, *Physical principles of medical imaging*. New York, NY, USA: Aspen Publishers, 1993.

[14] A. Mackenzie and I. D. Honey, “Characterization of noise sources for two generations of computed radiography systems using powder and crystalline photostimulable phosphors,” *Med. Phys.*, vol. 34, no. 8, pp. 3345–3357, 2007, doi: 10.1118/1.2750973.

[15] R. Bouwman, K. Young, B. Lazzari, V. Ravaglia, M. Broeders, and R. Van Engen, “An alternative method for noise analysis using pixel variance as part of quality control procedures on digital mammography systems,” *Phys. Med. Biol.*, vol. 54, no. 22, pp. 6809–6822, 2009, doi: 10.1088/0031-9155/54/22/004.

[16] A. Mackenzie, D. R. Dance, O. Diaz, and K. C. Young, “Image simulation and a model of noise power spectra across a range of mammographic beam qualities,” *Med. Phys.*, vol. 41, no. 12, 2014, doi: 10.1118/1.4900819.

[17] D. Sik, “High-precision noise power spectrum measurements in digital radiography imaging,” vol. 45, no. September, 2018.

[18] H. Alsleem and R. Davidson, “Quality parameters and assessment methods of digital radiography images,” *Radiographer*, vol. 59, no. 2, pp. 46–55, 2012, doi: 10.1002/j.2051-3909.2012.tb00174.x.

[19] I. D. Honey and A. MacKenzie, “Artifacts found during quality assurance testing of computed radiography and digital radiography detectors,” *J. Digit. Imaging*, vol. 22, no. 4, pp. 383–392, 2009, doi: 10.1007/s10278-008-9109-0.

[20] J. Beutel, J. M. Fitzpatrick, S. C. Horii, H. L. Kundel, and R. L. Van Metter, *Handbook of Medical Imaging, Volume 1. Physics and Psychophysics*. 2010.

[21] R. T. O. David A. Jimenez, Laura J. Armburst, “Artifacts In Digital Radiography,” *Vet. Radiol. ultrasound*, vol. 4, no. 49, pp. 321–332, 2008, doi: 10.1111/j.1740-8261.2008.00374.x.

[22] A. Walz-Flannigan, D. Magnuson, D. Erickson, and B. Schueler, “Artifacts in digital radiography,” *Am. J. Roentgenol.*, vol. 198, no. 1, pp. 156–161, 2012, doi: 10.2214/AJR.11.7237.

[23] E. Samei, M. J. Flynn, and D. A. Reimann, “A method for measuring the presampled MTF of digital radiographic systems using an edge test device,” *Med. Phys.*, vol. 25, no. 1, pp. 102–113, 1998, doi: 10.1118/1.598165.

[24] A. Kuhls-gilcrist, A. Jain, D. R. Bednarek, K. R. Hoffmann, and S. Rudin, “Accurate MTF measurement in digital radiography using noise response,” doi: 10.1118/1.3284376.

[25] A. Kuhls-Gilcrist, D. R. Bednarek, and S. Rudin, “A method for the determination of the two-dimensional MTF of digital radiography systems using only the noise response,” *Med. Imaging 2010 Phys. Med. Imaging*, vol. 7622, p. 76224W, 2010, doi: 10.1117/12.843918.

[26] A. Macovski, *Medical imaging systems*. 1983.

[27] International Electrotechnical Commission, “Medical electrical equipment—Characteristics of digital X-ray imaging devices—Part 1: determination of the detective quantum efficiency,” *IEC 62220-1 (Geneva IEC)*, vol. 2003, 2003.

[28] P. Monnin, H. Bosmans, F. R. Verdun, and N. W. Marshall, “Comparison of the polynomial model against explicit measurements of noise components for different mammography systems,” *Phys. Med. Biol.*, vol. 59, no. 19, pp. 5741–5761, 2014, doi: 10.1088/0031-9155/59/19/5741.

[29] N. W. Marshall, M. Smet, M. Hofmans, H. Pauwels, T. De Clercq, and H. Bosmans, “Technical characterization of five X-ray detectors for paediatric radiography applications,” *Phys. Med. Biol.*, vol. 62, no. 24, pp. N573–N586, 2017, doi: 10.1088/1361-6560/aa9599.

[30] Z. Zhou, F. Gao, H. Zhao, and L. Zhang, “Techniques to improve the accuracy of noise

power spectrum measurements in digital x-ray imaging based on background trends removal," *Med. Phys.*, vol. 38, no. 3, pp. 1600–1610, 2011, doi: 10.1118/1.3556566.

[31] P. Russo and G. Mettivier, "Method for measuring the focal spot size of an x-ray tube using a coded aperture mask and a digital detector," *Med. Phys.*, vol. 38, no. 4, pp. 2099–2115, 2011, doi: 10.1118/1.3567503.

[32] R. L. Wackerly, Dennis D., Mendenhall, William., and Scheaffer, *Mathematical Statistics with Applications*, 7th ed. Belmont, CA: Thomson Brooks/Cole, 2008.